(43)

# Characterization of Clouds in Atmospheric Temperature Profile Retrievals

by

Frederick Wey-Min Chen

Submitted to the Department of Electrical Engineering and Computer Science
in Partial Fulfillment of the Requirements for the Degrees of
Bachelor of Science in Electrical Science and Engineering
and Master of Engineering in Electrical Engineering and Computer Science
at the Massachusetts Institute of Technology

May 22, 1998



Author .....
Department of Electrical Engineering and Computer Science
May 22, 1998

Certified by .....
David H. Staelin
Thesis Supervisor

Accepted by .....
Arthur C. Smith
Chairman, Department Committee on Graduate Theses

Characterization of Clouds in Atmospheric Temperature Profile Retrievals
by
Frederick Wey-Min Chen

Submitted to the
Department of Electrical Engineering and Computer Science

May 22, 1998

In Partial Fulfillment of the Requirements for the Degrees of
Bachelor of Science in Electrical Science and Engineering
and Master of Engineering in Electrical Engineering and Computer Science

# ABSTRACT

Microwave emission spectra observed near the oxygen absorption line near 118 GHz and from above the earth's atmosphere can be used to determine a temperature profile. However, clouds can perturb brightness temperature measurements by over 100 K. One would like to locate and characterize clouds in order to correct the inferred temperature profile. This thesis presents a method for finding and characterizing clouds based on brightness temperature measurements.

The brightness temperatures measured by a downward looking radiometer aboard a high-altitude aircraft were filtered to reduce noise, and then warped so that the effects of strongly convected ice would not dominate the statistics of the emission spectra. The radiometer measured upwelling emission spectra at spots between -46.8° and +46.8° from nadir. In a cloud-free region of uniform temperature, the measured brightness temperatures typically are lower at spots away from nadir than at spots close to nadir. The average of the warped brightness temperatures in a region of clear air were computed and then subtracted from all of the warped brightness temperatures in order to eliminate cross-scan curvature from the data.

The resulting data was transformed into uncorrelated random variables using principal components analysis. The application of principal components analysis on all of the valid data showed that the degrees of freedom such as cloud cover, atmospheric temperature, and surface emissivity produced correlated effects in the data even though there was no reason to think that they were correlated. The first principal component was sensitive to cloud cover. However, it was sensitive also to variations in surface emissivity. A principal component that described the variations in surface emissivity was computed by applying principal components analysis on a set of data over cloud-free regions with varying surfaces. Then, that principal component was removed from the data. The first principal component of the resulting data, called the first post-constraint principal component, was sensitive to clouds but not to surface variations. A cloud flag index based on that principal component was formulated. However, it was found to be influenced by atmospheric temperature. The second post-constraint principal component was used to formulate another

cloud flag which was insensitive to atmospheric temperature variations.

This cloud flag was applied to about 11 hours of data from three flights during which the aircraft flew over some storm clouds. A comparison of the results with images of the earth's surface and of the morphology of the clouds taken for each flight showed that the cloud flag correctly characterized regions for two of the flights. For the third flight, the cloud flag did not perform as well due to, perhaps, differences between the calibrations for each flight.

Thesis Supervisor: David H. Staelin
Title: Professor of Electrical Engineering

# Acknowledgments

First, I would like to thank my Lord and Savior Jesus Christ for saving me and for giving me the strength to get through five years at MIT. I thank Him also for always being at my side and for making me a better person than the one I was before I knew Him personally.

I thank Prof. David H. Staelin for his guidance and for giving me the privilege of participating in his research.

I thank Bill Blackwell for his guidance and patience and for letting me contribute to the latest microwave temperature sounder (MTS).

I thank Prof. Louis D. Braida for giving me my first chance to participate in research.

I thank my parents for their love and their support. I'm glad that I have parents who encourage me and are willing to drive three hours to watch me perform.

I thank my grandparents for the love that they have shown me even though they live overseas. I'm very blessed to have grandparents who have given me a lot, even at least a year of tuition at MIT, even though they do not see me very often.

Lastly, I thank my brothers and sisters in Christ from the MIT Chinese Bible Fellowship and the Inter-Collegiate Fellowship of the Chinese Bible Church of Greater Boston for their encouragement and prayers and for making my years at MIT very enjoyable.

# Table of Contents

# List of Figures

# List of Tables

# Chapter 1

# Introduction

## 1.1 A Brief History of Research in Atmospheric Temperature Profile Retrieval Using Microwave Data

In the spring of 1998, the Remote Sensing Group at the Massachusetts Institute of Technology's Research Laboratory of Electronics completed the construction of a microwave temperature sounder (MTS). It measures the upwelling thermal radiation from the atmosphere at various microwave frequencies. The data that is collected by this MTS will be used to construct temperature profiles. The MTS that Gasiewski et al. (1990) constructed had an eight-channel scanning 118.75-GHz radiometer and a nadir-viewing 53.65-GHz spectrometer. The MTS that has just been completed has an eight-channel scanning 118.75-GHz radiometer and a nine-channel scanning 53.65-GHz radiometer and has been constructed with better components. These improvements should result in more accurate temperature profile retrievals. This research will support the development of improved methods for interpreting data and help determine the feasibility of passive microwave satellite-based spectrometers which yield useful atmospheric temperature profile retrievals.

## 1.2 Definition of the Problem

Cloud cover has been known to perturb brightness temperature measurements near 53 GHz and 118 GHz and other microwave frequencies. Staelin et al. (1975) investigated the effects of clouds on the data taken by the Nimbus-5 satellite. The instrument used in that investigation had five channels including a 53.65-GHz channel which was significantly affected by clouds. In 1986, Gasiewski et al. (1990) used a 118.75-GHz radiometer to perform temperature retrievals during the Genesis of Atlantic Lows Experiment (GALE) and the Cooperative Huntsville Meteorological Experiment (COHMEX) and found that the

118.75-GHz channels are somewhat more sensitive to clouds than the 53.65-GHz channels, as expected.

This thesis addresses the effects of clouds on temperature profile retrievals through the following two questions:

1. How do we determine the presence of a cloud?
2. What are the statistics of the effects of clouds?

Chapter 2 provides some technical background information that is relevant to this thesis; Chapter 3 describes the development of the cloud flag; and Chapter 4 summarizes the results of this research and makes suggestions for further research.

The appendixes show the results of applying the cloud flag to large samples of data.

# Chapter 2

# Background Information

## 2.1 Reasons Why Microwave Temperature Sounding is Possible

Matter radiates power based on its physical temperature. The amount of radiation that a blackbody radiates is given by

$$I = \frac{2hf^3}{c^2(e^{(hf)/(kT)} - 1)} \frac{W}{m^2 \cdot Hz \cdot ster} \tag{2.1}$$

where f is frequency, T is physical temperature, and $I$ is called the radiation intensity of a body. Real bodies are not blackbodies. The amount of energy radiated by a real body differs from the above formula by a scaling factor less than unity called the emissivity.

A radiometer on an airplane can look downward to measure the amount of upwelling thermal radiation from the atmosphere. Suppose that the atmosphere were divided horizontally into layers. Each layer would contribute to the radiation measured by each channel of the radiometer according to its weighting function. The weighting functions peak at specific altitudes. Therefore, we can construct temperature profiles that tell us temperature not only as a function of location along the flight path, but also as a function of altitude (Staelin 1974, Tsang et al. 1985).

## 2.2 Reasons for Using a 118.75-GHz Radiometer

118.75 GHz is a resonance frequency of the oxygen molecule $O_2$. Oxygen is well-mixed throughout the atmosphere, so one can use the brightness temperature of oxygen to determine physical temperature profiles (Staelin 1997).

## 2.3 Principal Components Analysis

Principal components analysis transforms a set of random variables into a set of uncorrelated random variables called principal components. Suppose that an N-dimensional ran-

dom vector **x** with covariance $\Lambda_x$ is given.

$$\mathbf{x} = \begin{bmatrix} x[1] \\ x[2] \\ \cdots \\ x[N] \end{bmatrix} \tag{2.2}$$

$$\Lambda_x = \begin{bmatrix} \lambda_{11} & \lambda_{12} & \cdots & \lambda_{1N} \\ \lambda_{21} & \lambda_{22} & \cdots & \cdots \\ \cdots & \cdots & \cdots & \cdots \\ \lambda_{N1} & \cdots & \cdots & \lambda_{NN} \end{bmatrix} \tag{2.3}$$

$\lambda_{ij}$ is the covariance between x[i] and x[j]. The covariance of two random variables y and z is given by the following equation:

$$\mathrm{Cov}(y,z) = E[(y - E(y))(z - E(z))] \tag{2.4}$$

where E is the expected value of a random variable. One wishes to find a matrix **Q** such that

$$\mathrm{Var}(\mathbf{Qx}) = \mathbf{Q}\Lambda_x\mathbf{Q}^T \tag{2.5}$$

is a diagonal matrix. The matrices that will diagonalize the covariance matrix $\Lambda_x$ are the matrices whose columns are the eigenvectors of $\Lambda_x$. The elements of **Qx** are the principal components of **x** (Helstrom 1991). The first principal component is the one with the largest eigenvalue; the second principal component is the one with the second largest eigenvalue; and so on.

**2.3.1** Applying Principal Components Analysis to Cloud Characterization

This thesis describes the analysis of data collected using the MTS constructed by Gasiewski et al. (1990) which had an eight-channel scanning 118.75-GHz radiometer. Because there are eight measurements for each location, eight principal components will be determined.

Factors that affect the amount of power radiated by the atmosphere include cloud cover, surface emissivity, humidity, and atmospheric temperature. Atmospheric tempera-

ture does not vary greatly over horizontal distance since the autocorrelation function of temperature over horizontal distance is non-negligible for separations up to 2000 km (Nathan et al. 1985). Clouds make the biggest contributions to brightness temperature variations and appear in two-dimensional brightness temperature plots as localized depressions. Precipitating clouds with ice can perturb brightness temperature measurements by over 100 K (Gasiewski et al. 1990). Because clouds can produce such large perturbations, information about cloud cover will probably be contained in the first few principal components of the brightness temperature measurements.

# Chapter 3

# Development of the Cloud Flag

## 3.1 Description of the Data

The data that was used in the development of the cloud flag was collected on October 5, 1993, by the old MTS while it was aboard one of the National Aeronautics and Space Administration's (NASA) ER-2 high-altitude aircraft flying at an altitude about 20 km above sea level. The aircraft flew over the southeastern U.S. The available data included radiometric data, a videotape of the surface of the earth along the flight path, and navigational information. The videotape and the navigational information were used to determine the accuracy of the cloud flag. At each point along the flight path, the old MTS took measurements at fourteen uniformly spaced spots between -46.8° to +46.8° from nadir covering 40 km at the surface of the earth (Schwartz et al. 1996). The spot at -46.8° from nadir (to the right of the aircraft) will be called spot 1, and the spot at +46.8° (to the left of the aircraft) from nadir will be called spot 14.

The channels are described as follows by Schwartz et al. (1996):

> "The eight MTS channels have double-sideband passbands symmetrically spaced from 470 to 1880 MHz from the line center [118.75 GHz], with widths ranging from 170 to 290 MHz."

| Channel | Sideband Frequencies (GHz) |
|---|---|
| 1 | 118.75 ± 0.65 |
| 2 | 118.75 ± 0.82 |
| 3 | 118.75 ± 1.03 |
| 4 | 118.75 ± 1.24 |
| 5 | 118.75 ± 1.46 |
| 6 | 118.75 ± 1.68 |
| 7 | 118.75 ± 1.88 |
| 8 | 118.75 ± 0.47 |

**Table 3.1: The Sideband Frequencies of the Channels of the MTS**

## 3.2 Initial Processing of the Radiometric Data

### **3.2.1** First Step: Filtering the Data

The data was noisy, so the first step in processing the data was to spatially filter all of the data with the following set of filter coefficients:

$$h = \begin{bmatrix} h[-1,1] & h[0,1] & h[1,1] \\ h[-1,0] & h[0,0] & h[1,0] \\ h[-1,-1] & h[0,-1] & h[1,-1] \end{bmatrix} = \begin{bmatrix} 1 & 2 & 1 \\ 2 & 3 & 2 \\ 1 & 2 & 1 \end{bmatrix} \tag{3.1}$$

The first index is the scan number, and the second is the spot number.

### **3.2.2** Second Step: Warping the Data

Precipitation and ice can perturb brightness temperature measurements by over 100 K (Gasiewski et al. 1990). Warping the data will prevent ice signatures from dominating the

statistics of the brightness temperature measurements. Here the original brightness temperature T is warped to T' using the following equation:

$$T' = T + \frac{(T_{max} - T)^2}{500} \tag{3.2}$$

$T_{max}$ is an upper bound on the measured brightness temperatures. The highest observed brightness temperature was about 270 K, so $T_{max}$ was chosen to be 300 K. For observed brightness temperatures between 250 K and 300 K, the warping function does not change the brightness temperature by more than 5 K, so small perturbations are not significantly changed. In regions with precipitating clouds and ice, the warping function will significantly reduce perturbations. For example, if the observed brightness temperature at a spot is 180 K, as it might be in a region with precipitation, the warping function will increase the brightness temperature by 28 K (Figure 3.1).

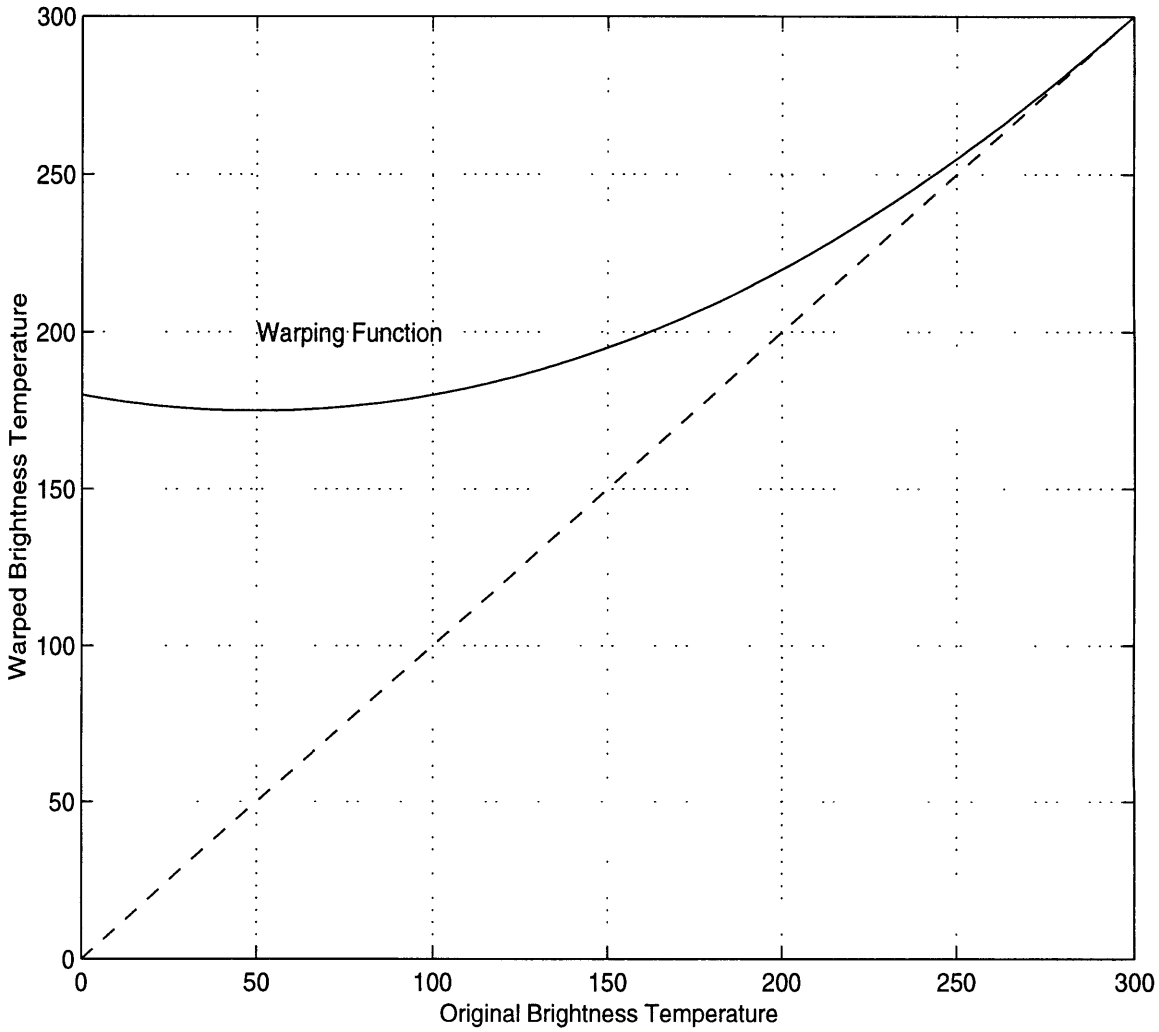


**Figure 3.1:** The Warping Function

**3.2.3** Third Step: Removing Cross-Scan Curvature From the Data

Brightness temperature measurements typically are lower at spots 1 and 14, which are located at the extremes of a scan, than at spots 7 and 8, which are located close to nadir. Figure 3.2 shows a sample of the variation in warped brightness temperature associated with Channel 1 through one scan of clear air.

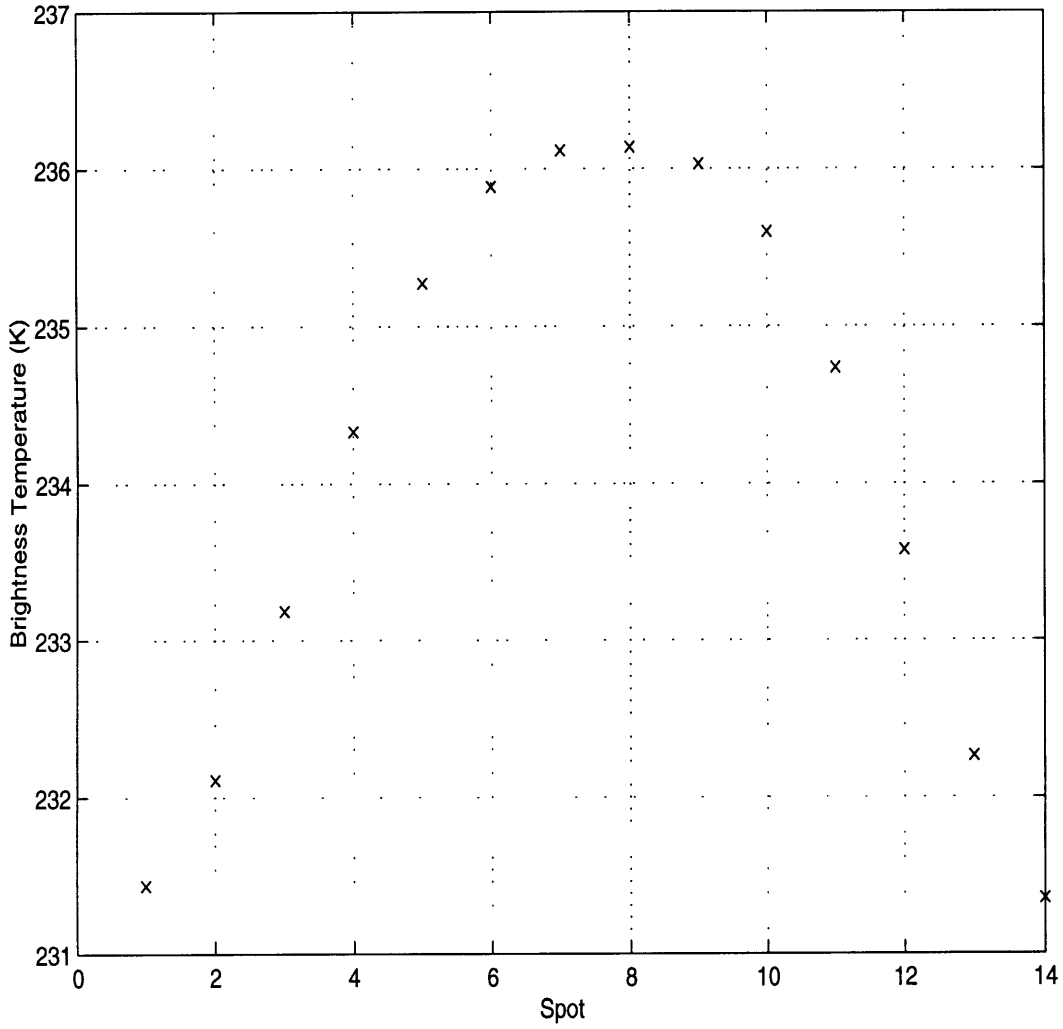


**Figure 3.2:** Cross-Scan Curvature of Warped Brightness Temperatures

When doing statistical analysis, developing a separate cloud flag for each spot is undesirable, so it is necessary to subtract an average of the warped brightness temperatures at each spot. The averages were calculated over a cloud-free region of land. Figure 3.3 shows the result for the data shown in Figure 3.2.

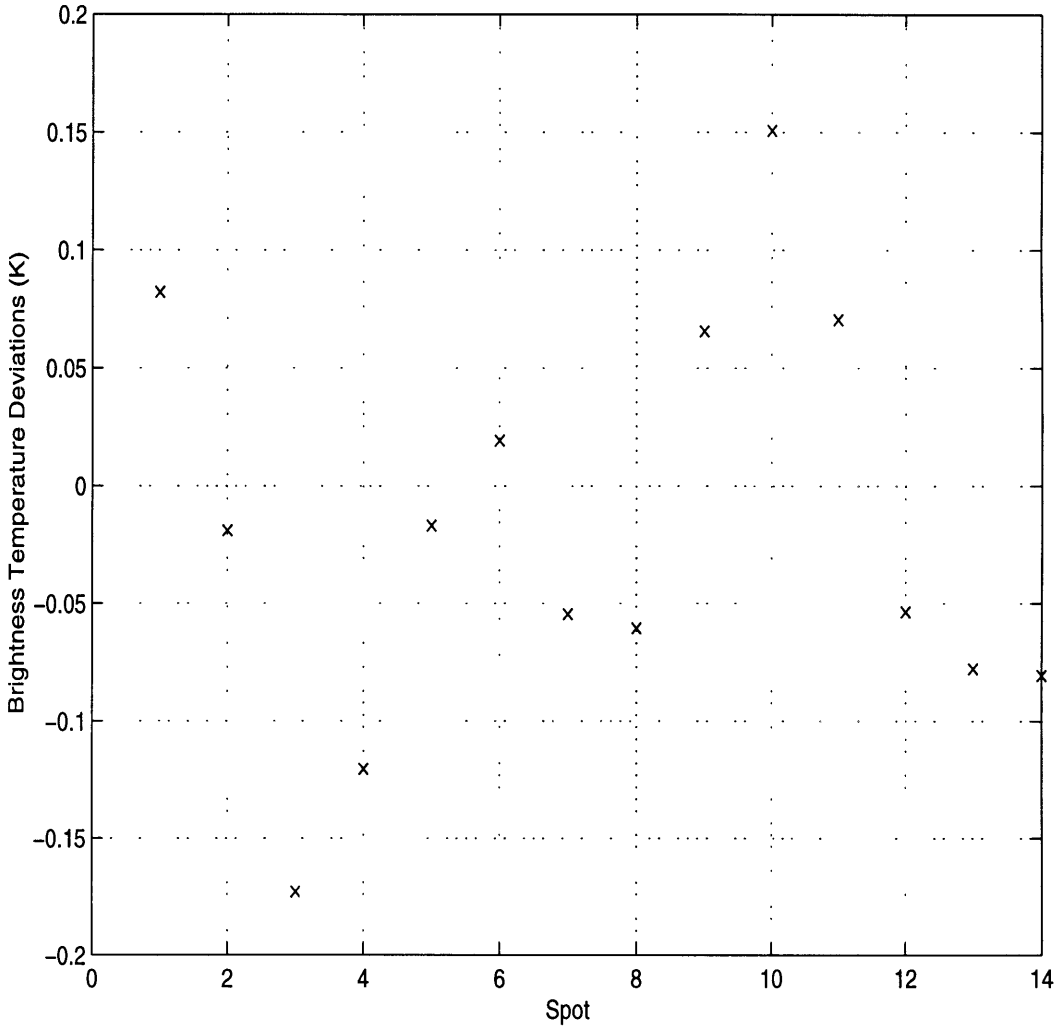


**Figure 3.3:** Brightness Temperature Deviations Across One Scan

The result appears to be random noise. These brightness temperature deviations will be used to formulate the cloud flag.

## 3.3 Initial Results of Principal Components Analysis

Several degrees of freedom affect the brightness temperature observed by a radiometer. These include physical temperature, the effects of clouds, atmospheric humidity, and surface emissivity. Because these degrees of freedom are largely independent, principal components analysis should be able to separate the data at each spot into principal components

that describe the contribution that each degree of freedom makes to the data. Clouds cause the largest perturbations in the data. Therefore, the first principal component should be the one characterizing the contribution that clouds make to the data. Figure 3.4 shows the eigenvalues of the principal components of the brightness temperature deviations.

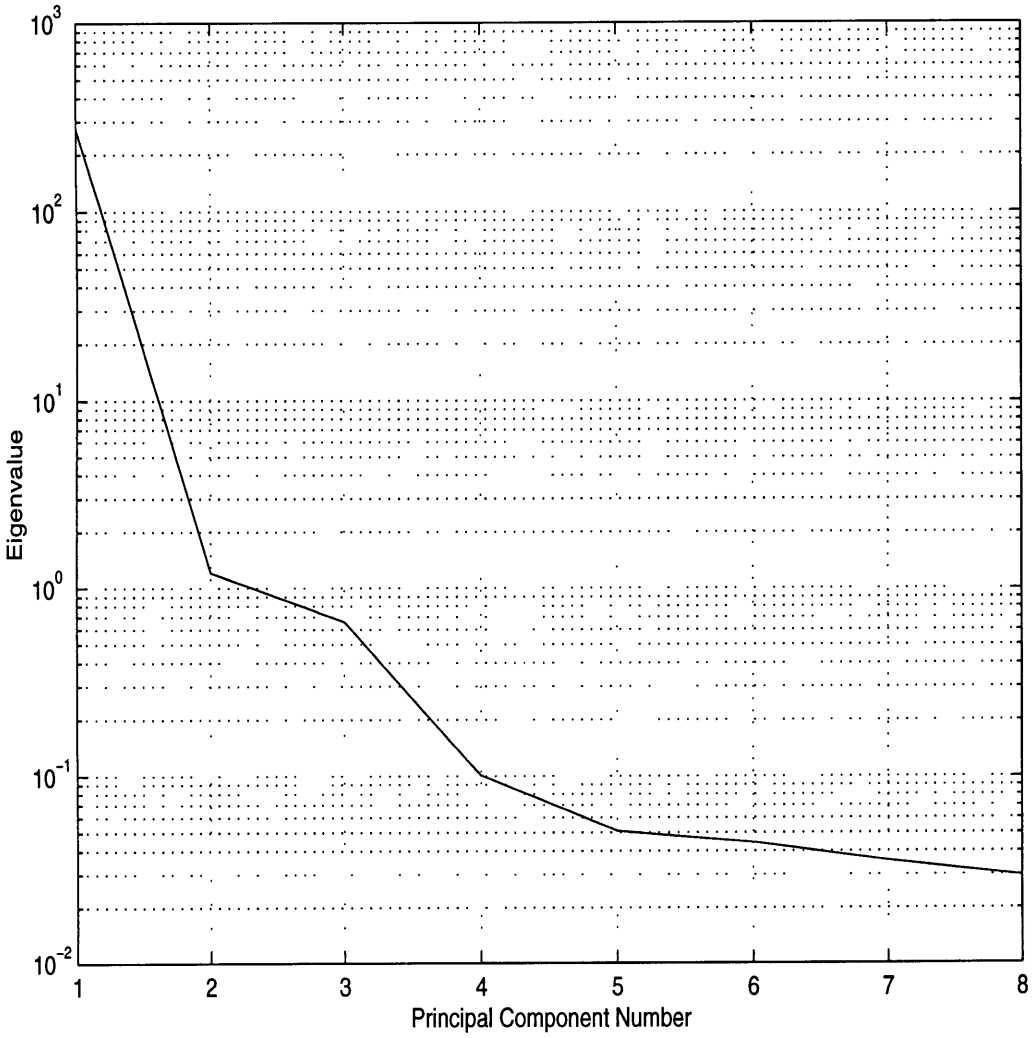


**Figure 3.4:** Eigenvalues of Principal Components of Brightness Temperature Deviations

Only the first three principal components make significant contributions to the data. Figures 3.5 and 3.6 show contour plots of each principal component over clear air and over cloudy air, respectively. Each strip is 40 km wide at the surface of the earth. For every

contour plot, distance is defined as the UTC time of day in seconds multiplied by 0.21 km/s, the speed of the aircraft.

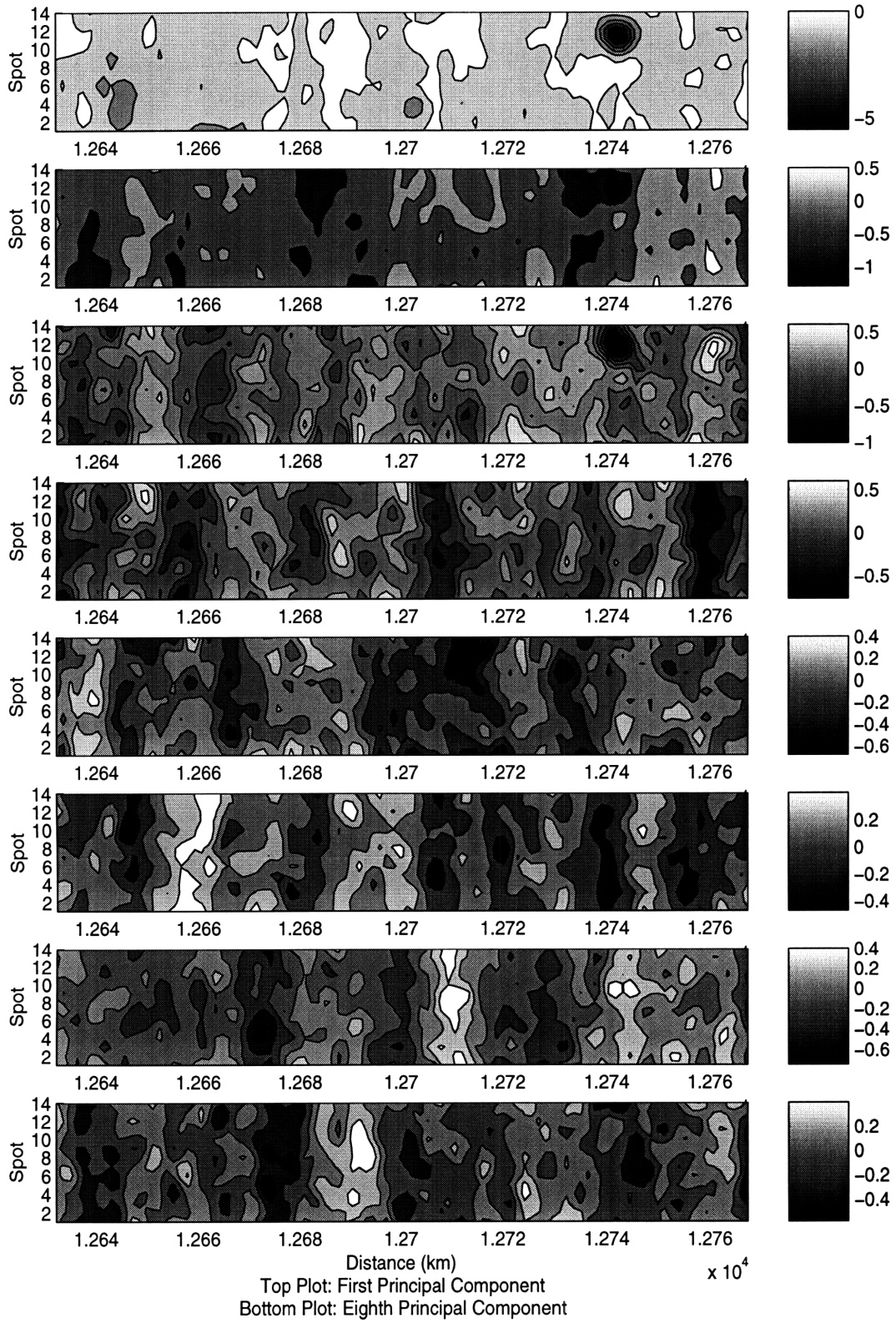


**Figure 3.5:** Principal Components Over Clear Air

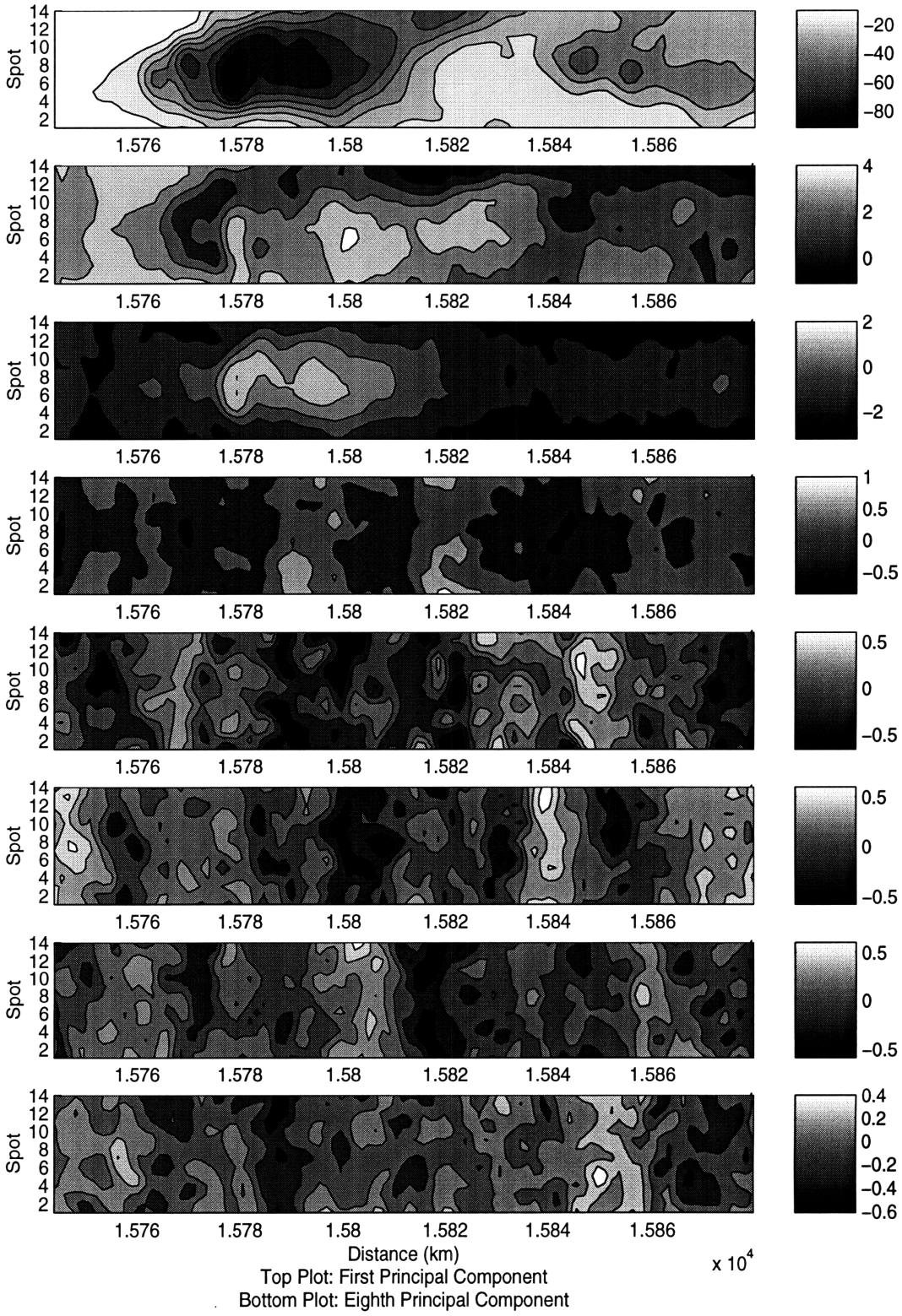


**Figure 3.6:** Principal Components Over Cloudy Air

One can see a difference between the plots of the principal components in clear air and in cloudy air. The clouds appear in the first three principal components. The last five principal components appear to be the result of calibration noise since there are vertical bars in the contour plots of those principal components. Because of this and because the eigenvalues associated with the last five principal components are insignificant when compared to the first three, one can ignore them. Subsequent sets of contour plots of principal components will show the contour plots for at most the first three principal components.

Although the first principal component is able to detect clouds, it is not a perfect cloud flag. In addition to clouds, it responds also to variations in surface emissivity. The small set of concentric circles in the contour plot of the first principal component of Figure 3.5 resulted from a lake. Therefore, the first principal component probably will also show land-sea boundaries. Variations in surface emissivity will not produce perturbations that big clouds can produce, but since they can mimic small clouds, any good cloud flag must be blind to variations in surface emissivity.

## 3.4 Constrained Principal Components Analysis

Surface emissivity and the presence of clouds should be uncorrelated. Unfortunately, applying principal components analysis on the entire set of brightness temperature deviations did not separate the effects of clouds from those of variations in surface emissivity. However, one can suppress information about surface variations by first determining the principal component that responds to surface variations and then removing that component from the data.

When determining the surface variation principal component, one must first choose a subset of the data on which to do principal components analysis. This subset will be called the training set. To suppress the contributions of surface variations to the cloud flag, one

should choose surface-variation training data over cloud-free regions that have different types of surfaces (e.g., grassland, swamps, mountains, ocean, etc.). The training set contained the lake in Figure 3.5 and a land-sea boundary. Figure 3.7 shows the covariances of the principal components that were computed.

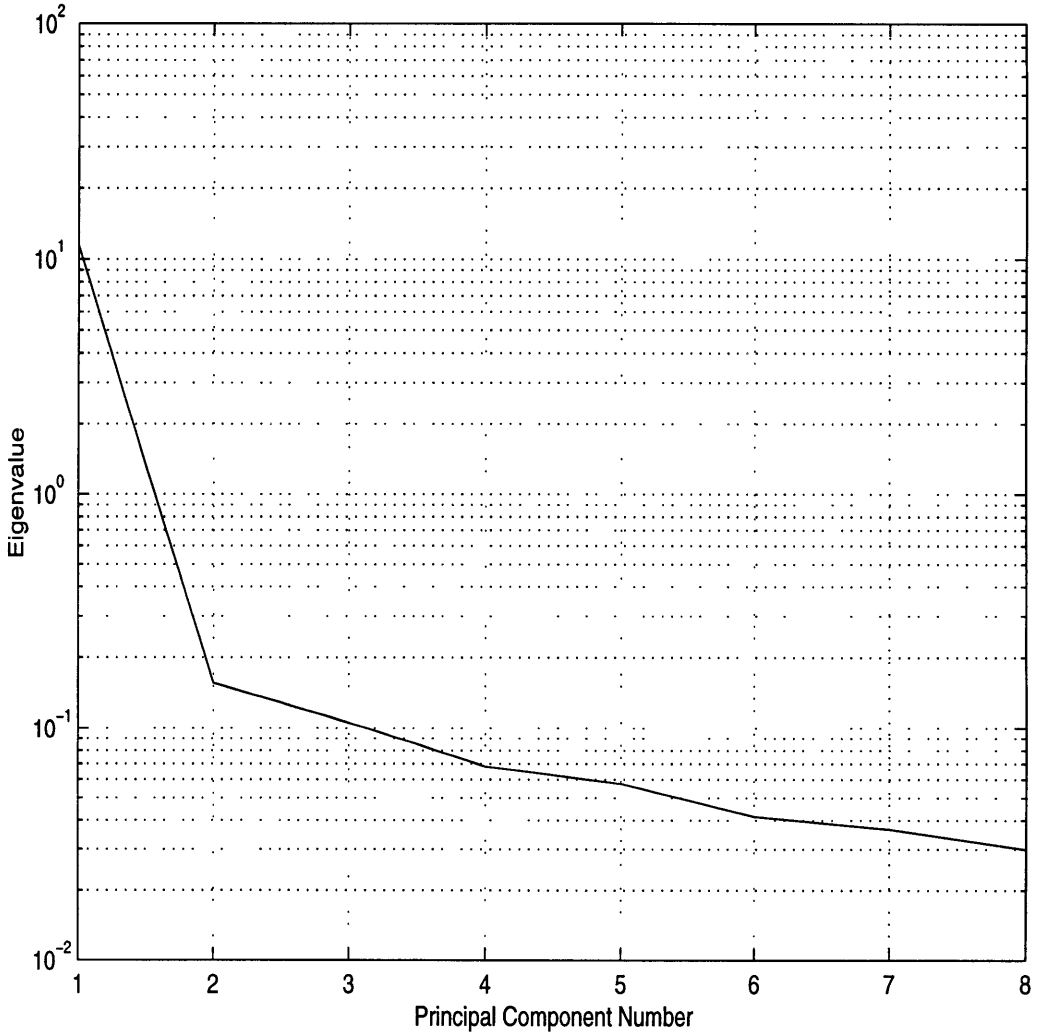


**Figure 3.7:** Eigenvalues of Principal Components of Data Over Clear Air

The first principal component captures nearly all of the variance of the data for clear air. Its variance is almost two orders of magnitude greater than that of the second principal

component. Figure 3.8 shows the principal components over the region described in Figure 3.5.

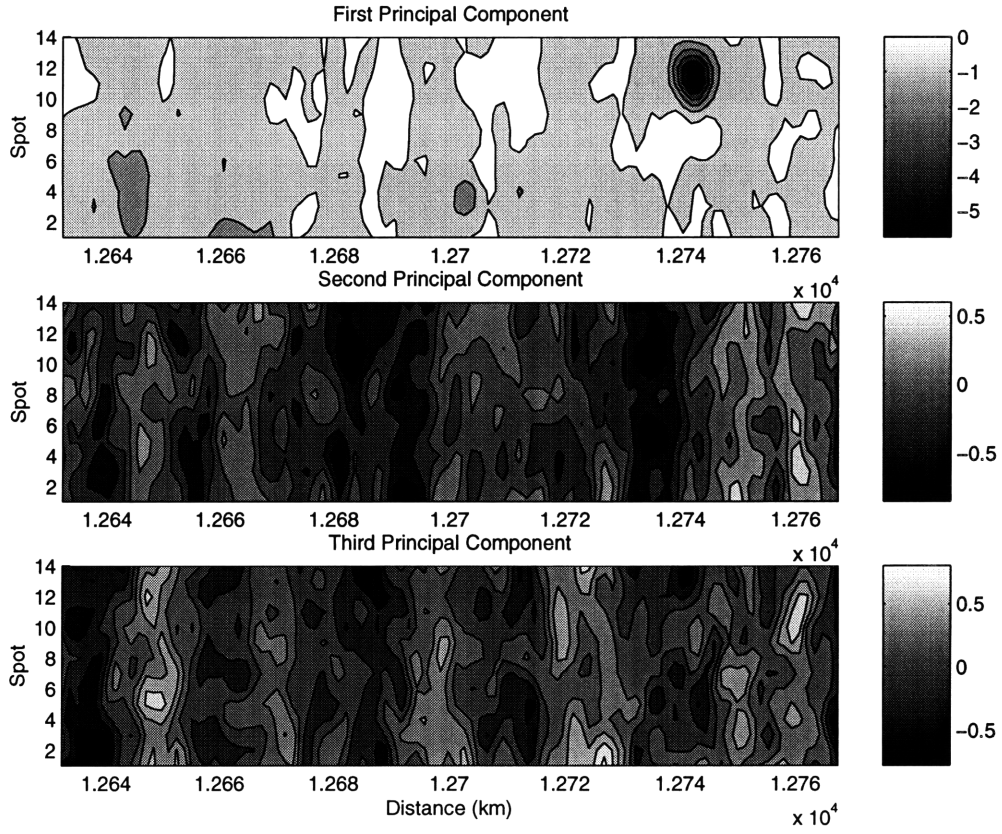


**Figure 3.8:** Principal Components Over a Lake

The first principal component detects the lake, as the concentric circles in the contour plot show. However, the lake does not appear in either the second or the third principal component. Therefore, removing the projection of the data onto the vector space spanned by only the first eigenvector, which will be called the surface variation eigenvector, should eliminate the effects of surface variations. Figure 3.9 shows the result of applying this step to the data described in Figure 3.8.

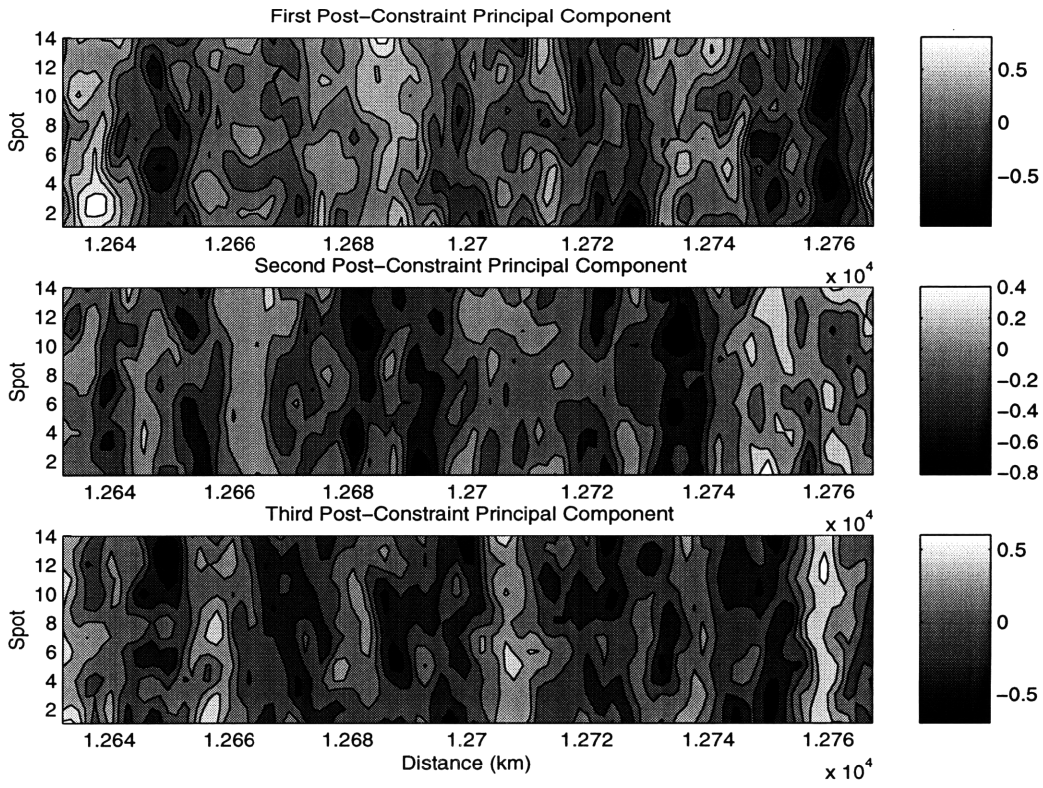


**Figure 3.9:** Post-Constraint Principal Components Over a Lake

The lake that was in the first principal component of the unconstrained data does not appear in the contour plots of the post-constraint principal components. If one were to see signs of surface variations in the second principal component, then one might remove the projection of the data onto the vector space spanned by the first two eigenvectors. Figure 3.10 shows the first three principal components of the unconstrained data over a region with a land-sea boundary, and Figure 3.11 shows the first three post-constraint principal components over the same region.

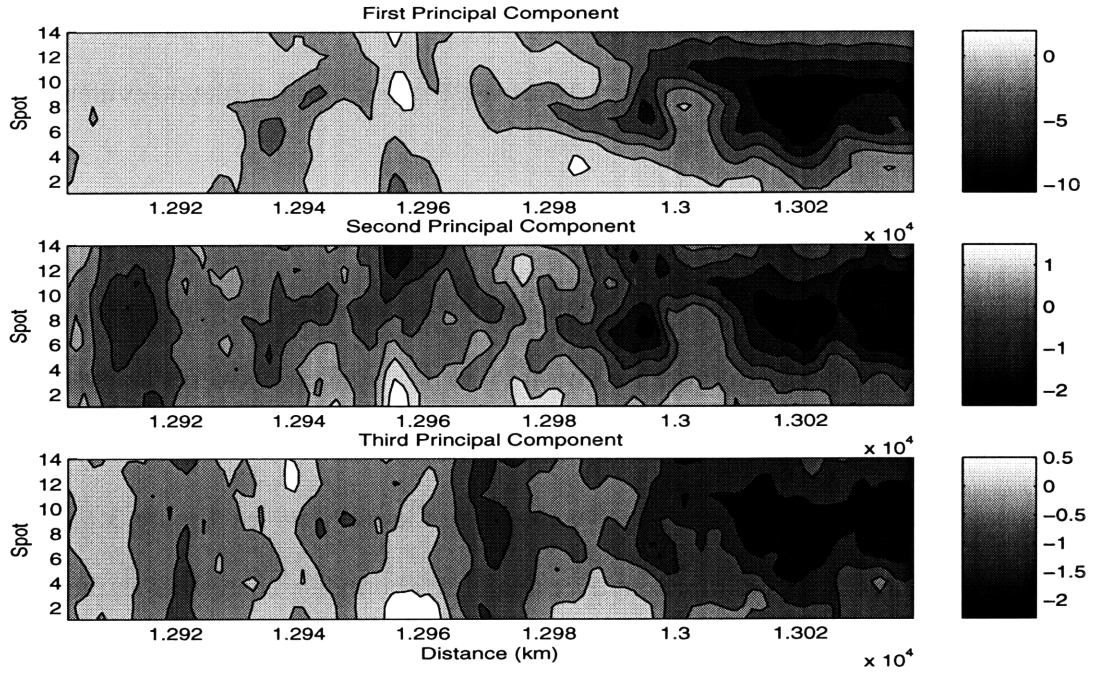


**Figure 3.10:** Pre-Constraint Principal Components Over Land-Sea Boundary

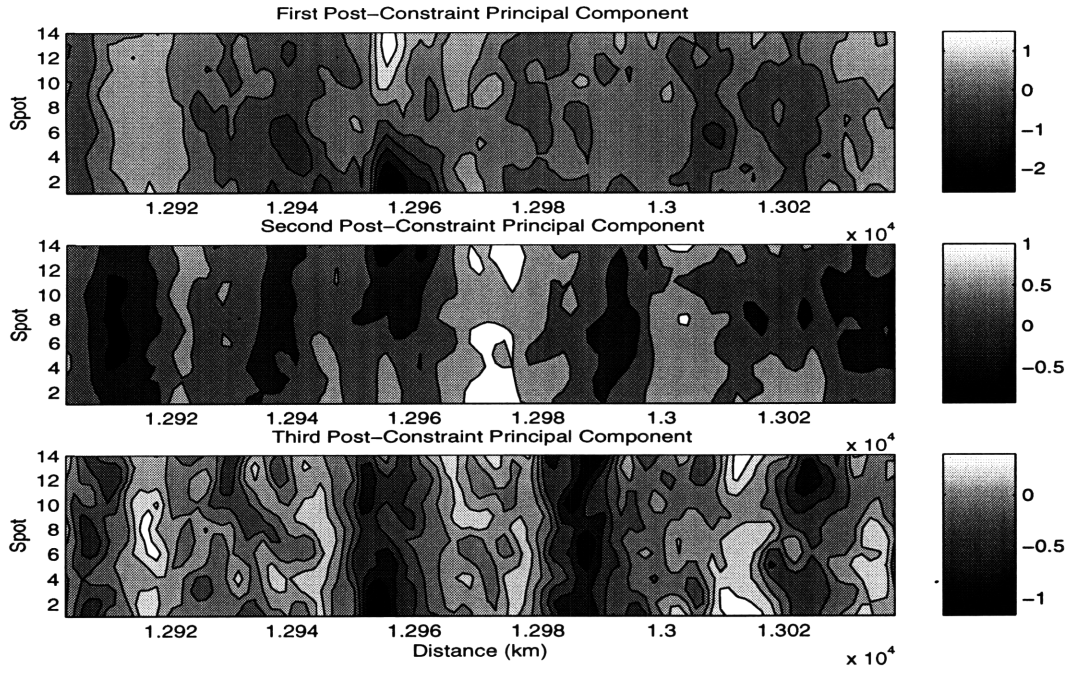


**Figure 3.11:** Post-Constraint Principal Components Over Land-Sea Boundary

The contour plot of the first principal component of Figure 3.10, shows a land-sea boundary when the distance is about 13000 km. Before this point the airplane is over land, and after this point the airplane is over sea. However, Figure 3.11 exhibits no evidence of a land-sea boundary.

Figures 3.9 and 3.11 show that some of the effects of surface variations have been removed from the data. This is not surprising since both examples of surface variations were part of the training set. In order for constrained principal components analysis to be useful, it must eliminate not only the effects of surface variations in regions included in the training set, but also those in regions not included in the training set. Figure 3.12 shows the same first three principal component over a land-sea boundary that is not in the region included in the training set. Before the distance is 17070 km, the plane is over sea, and afterwards, the plane is over land.

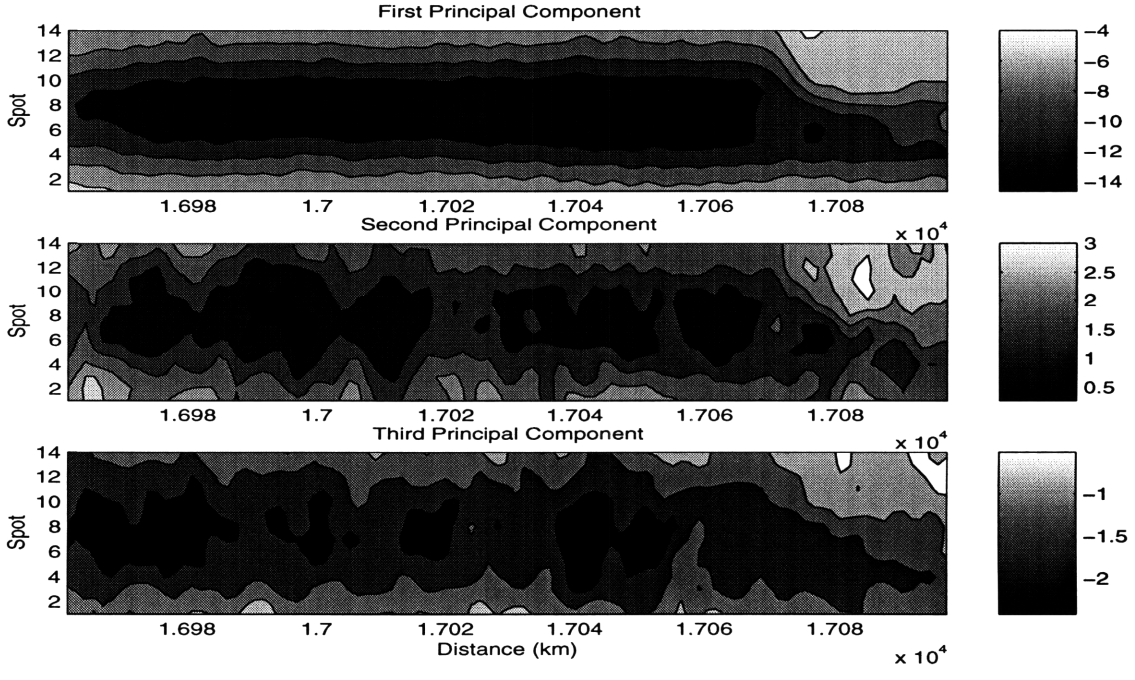


**Figure 3.12:** Pre-Constraint Principal Components Over Land-Sea Boundary Not in Training Set

Figure 3.13 shows the result of removing the component spanned by the surface variation eigenvector from the data over the same region.

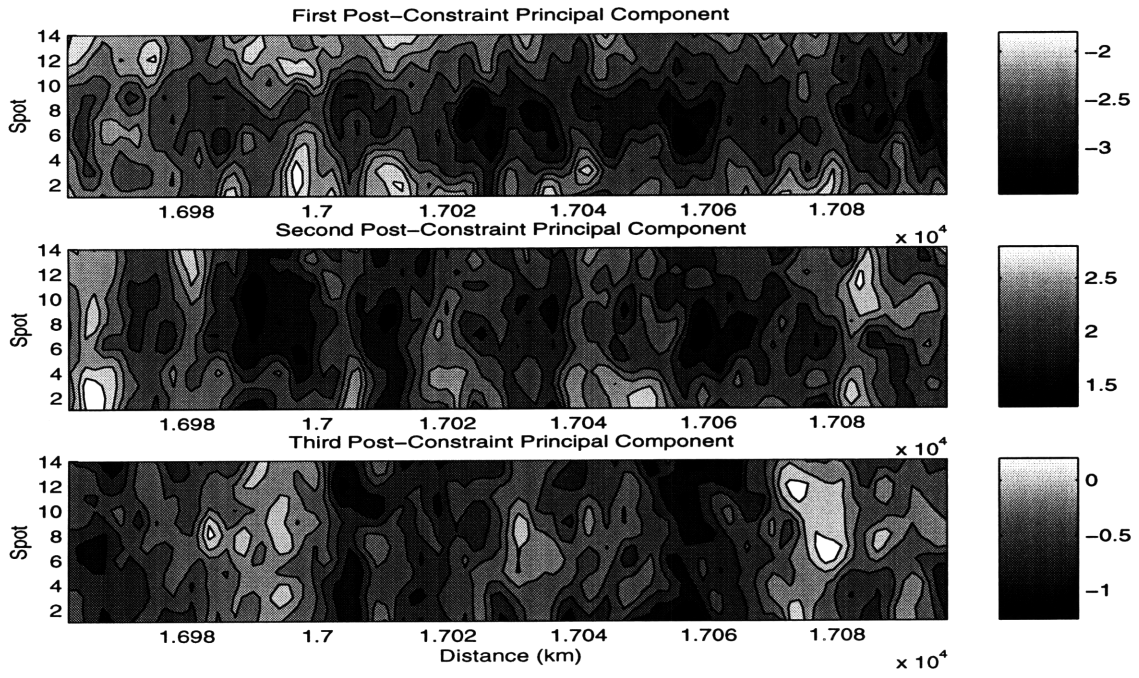


**Figure 3.13:** Post-Constraint Principal Components Over Land-Sea Boundary Not in Training Set

Since the land-sea boundary did not appear in the first post-constraint principal component, one can conclude that the effects of surface variations have been removed from the data. Removing the effects of surface variations should not also completely degrade information about cloud cover. Figure 3.14 shows the first three post-constraint principal components over the cloudy region described in Figure 3.6.

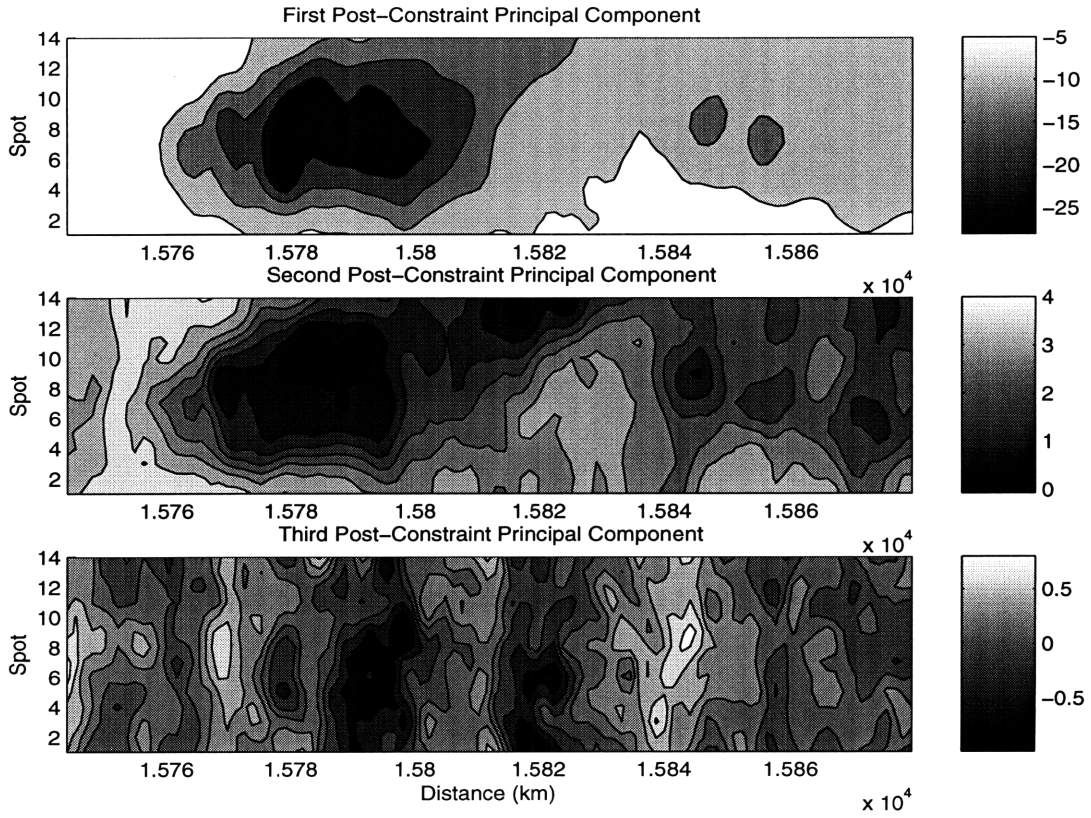


**Figure 3.14:** Post-Constraint Principal Component Over Cloudy Region

Although the first post-constraint principal component does not respond to surface variations, it still responds to clouds, although not quite so strongly.

Removing the surface variations component from the data eliminates the effects of surface variations but does not also eliminate information about clouds, so one can formulate a cloud flag based on the first post-constraint principal component.

## 3.5 A Cloud Flag Based on the First Post-Constraint Principal Component

Clouds are rare, so a cloud flag should indicate the absence of a cloud most of the time. Figure 3.15 shows a histogram of the first post-constraint principal component.

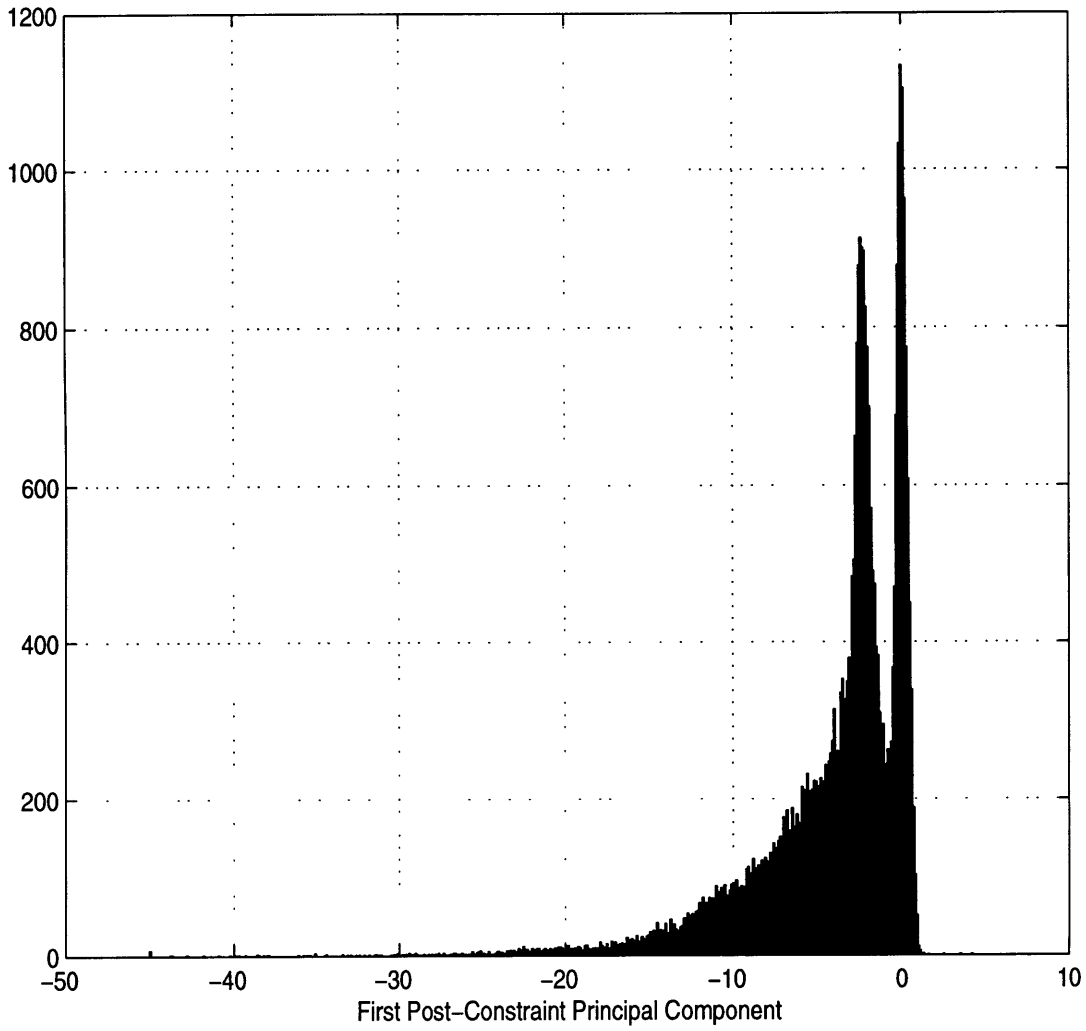


**Figure 3.15:** Histogram of First Post-Constraint Principal Component

Presumably, the spike to the right represents clear air, and the spike to the left represents areas of light cloud cover. The range of the cloud flag index can be divided into a range that indicates no cloud cover and one that indicates cloud cover. The two spikes suggest that all values greater than -1 would indicate the absence of a cloud. This results in the following cloud flag index:

$$-1 * (x + 1) \tag{3.3}$$

where x is the first post-constraint principal component. A cloud flag index less than zero indicates the absence of a cloud, and increasing indexes indicate increasing degrees of

cloud cover (Figure 3.16).

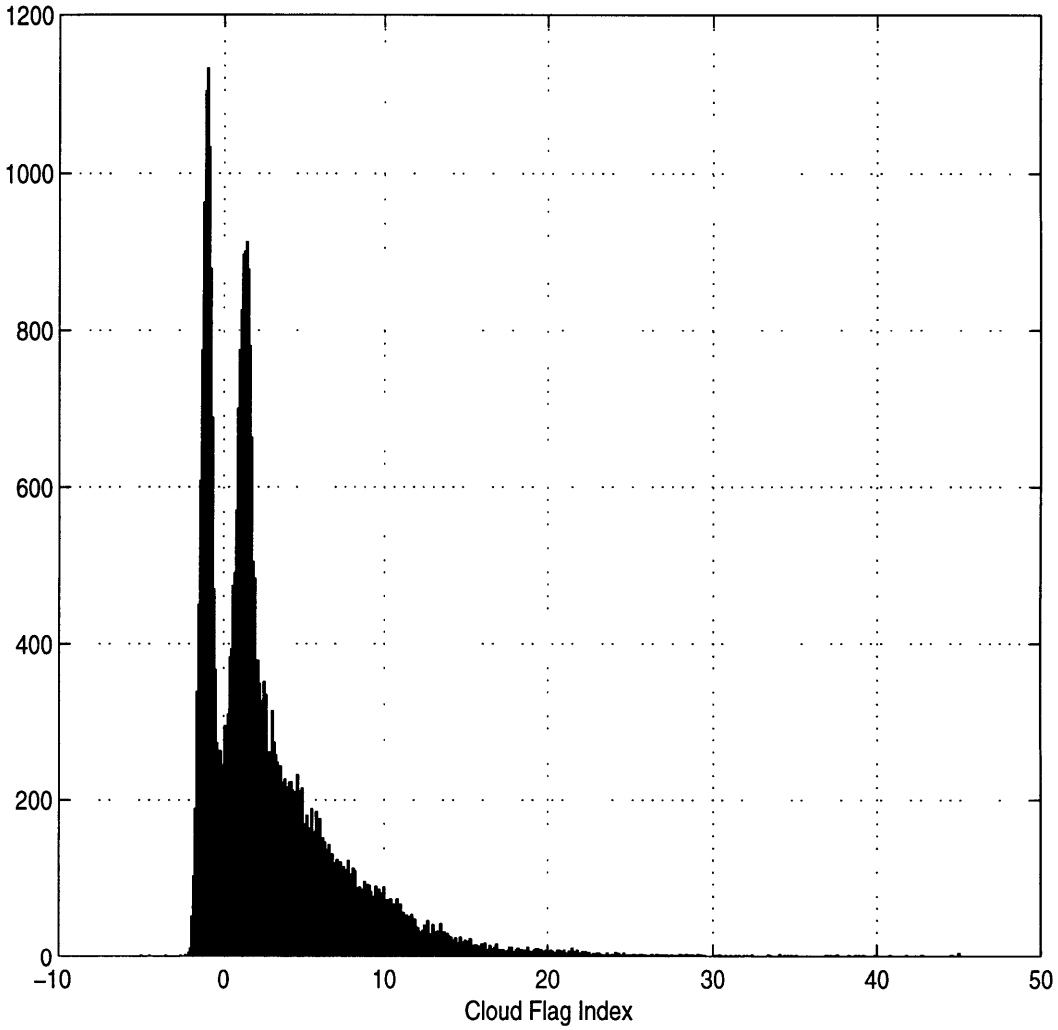


**Figure 3.16:** Histogram of Cloud Flag Index

This index correctly characterized warm clear air and large clouds. Figure 3.17 shows a contour plot of the cloud flag index over the cloudy region described in Figures 3.6 and 3.14.

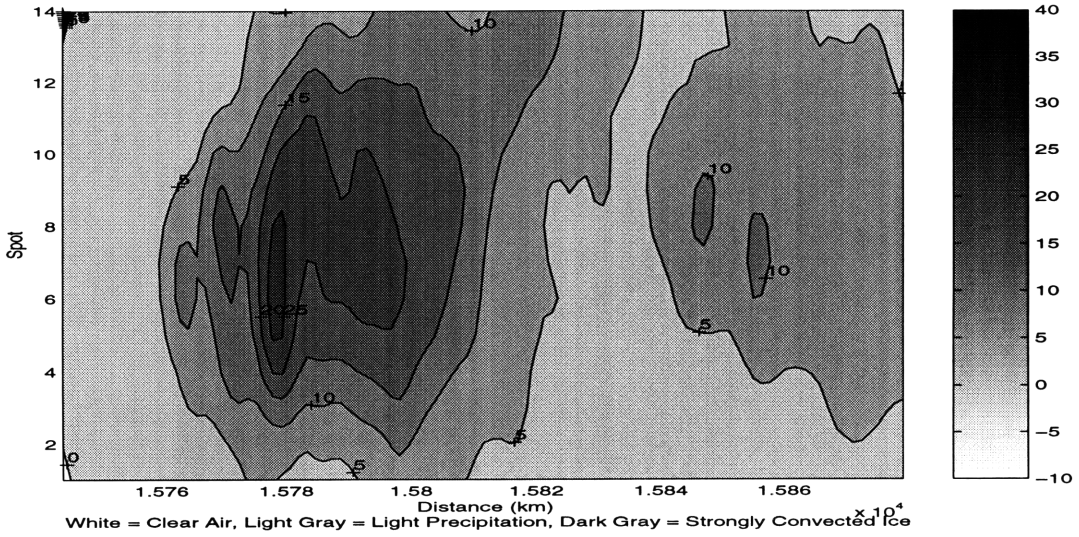


**Figure 3.17:** Plot of Cloud Flag Index in Cloudy Air

However, this cloud flag index is not perfect. The videotape showed that the surface of the earth was visible just before 15760 km, yet the cloud flag index indicates the presence of light precipitation. It also labels regions of cool clear air as regions with light cloud cover.

## 3.6 A Cloud Flag Based on the First Two Post-Constraint Principal Components

A cloud flag must be insensitive to not only the effects of surface variations, but also to changes in temperature. Constrained principal components analysis eliminated the effects of surface variations. However, the cloud flag based on the first post-constraint principal component was influenced by temperature. The second post-constraint principal component might provide some additional information that will improve the cloud flag. Figure 3.18 shows a scatter plot of the first and second post-constraint principal components.

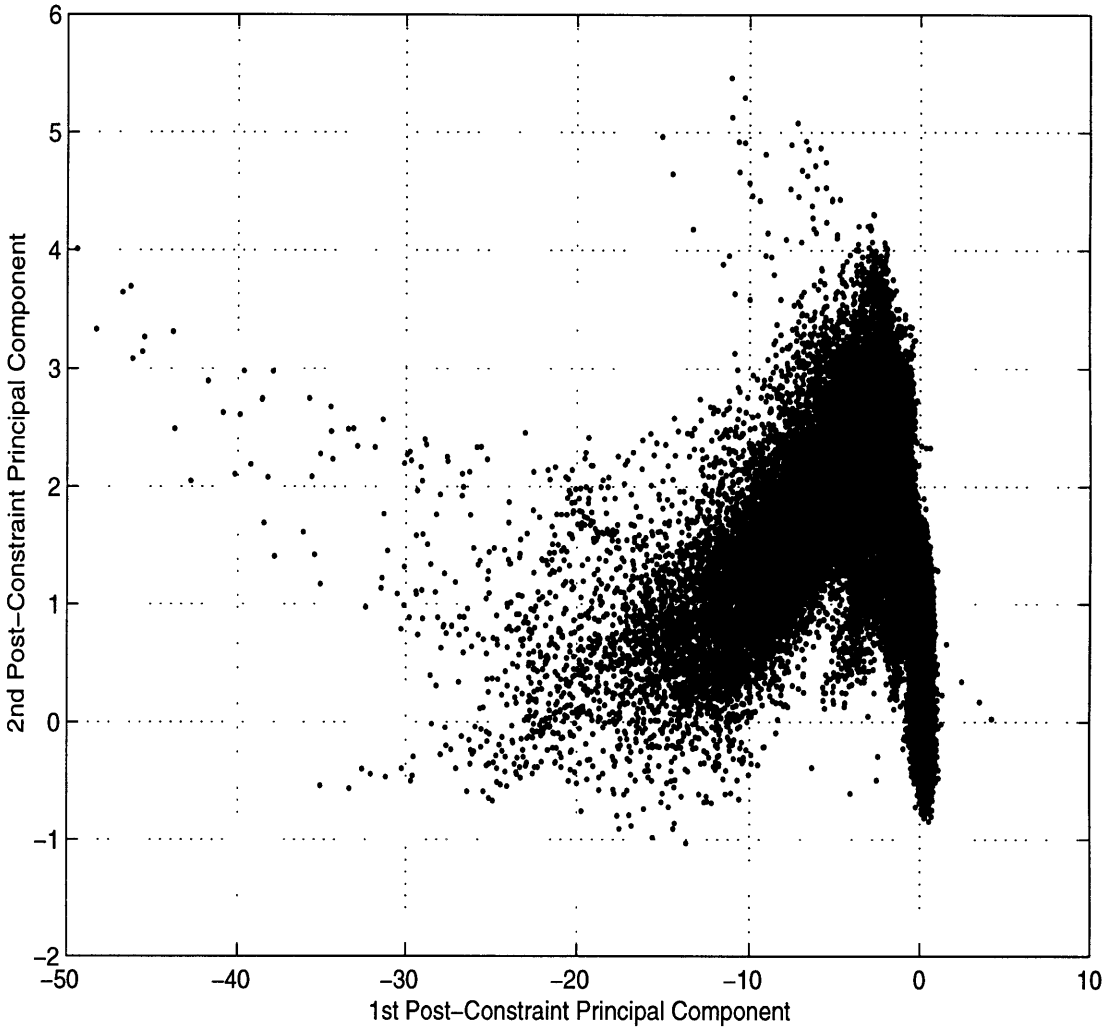


**Figure 3.18:** Scatter Plot of First Two Post-Constraint Principal Components

By plotting points in regions with specific characteristics, one can learn how individual factors affect each principal component. Figure 3.19 shows a scatter plot of the first two post-constraint principal components in warm clear air and cool clear air.

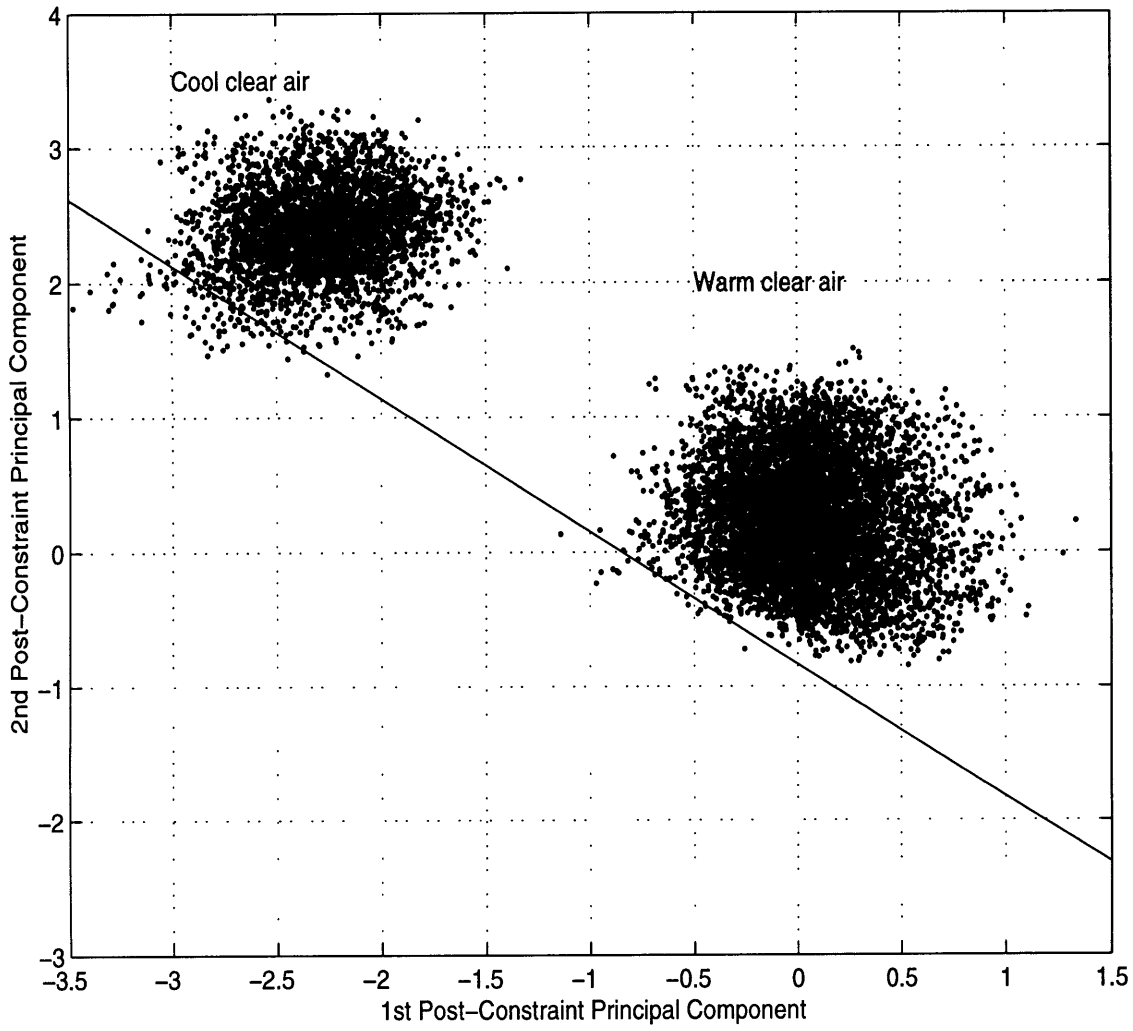


**Figure 3.19:** Scatter Plot for Warm Clear Air and Cool Clear Air

The points that result from cool clear air and those that result from warm clear air occupy opposite sides of the steep descent that is on the right side of Figure 3.18. This suggests that one might draw a line to divide the plot into regions of clear air and regions with cloud cover (Figure 3.19). If we assume that the effects of temperature variations and the effects of cloud cover are uncorrelated, then we can use other lines that are parallel to that line to divide the plot into regions of varying cloud cover. The slope of the lines will provide the information with which one can make a cloud flag index. For this set of data, the line that divides the 2-D space into regions of cloud cover and regions of clear air is

$$y + 0.9863\,x = -0.8350 \tag{3.4}$$

where x and y are the first and second post-constraint principal components, respectively. The region of the 2-D scatter plot that represents cloud cover can be further divided into regions of varying degrees of cloud cover by lines of the following form:

$$y + 0.9863\,x = c \tag{3.5}$$

where c is a constant less than -0.8350. So that the cloud flag index will indicate the absence of a cloud if and only if the index is less than zero and so that increasing index values will indicate increasing degrees of cloud cover, one can define the following cloud flag index:

$$-1 * (y + 0.9863\,x + 0.8350) \tag{3.6}$$

Figure 3.20 shows the scatter plot of the first two post-constraint principal components with contour lines for the cloud flag index.

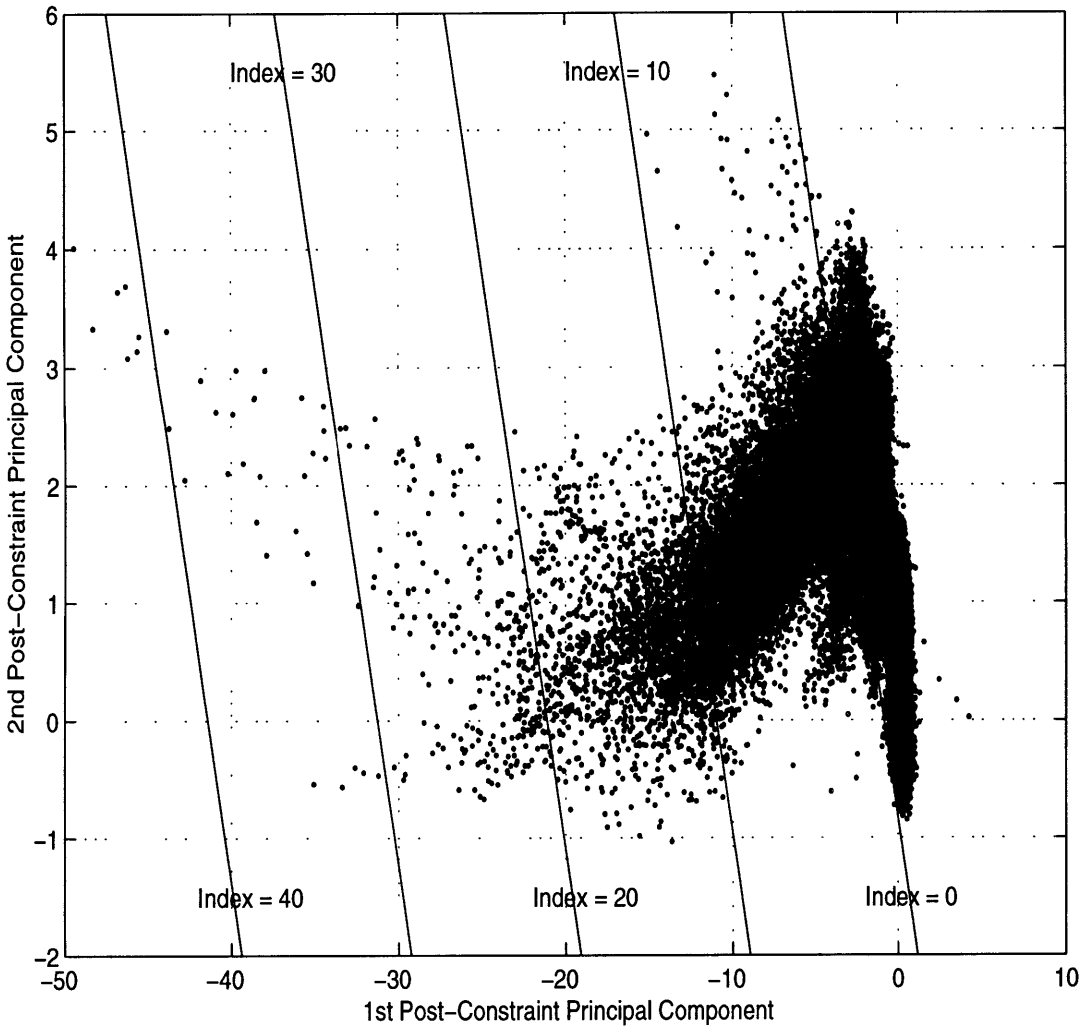


**Figure 3.20:** Scatter Plot With Contour Lines For Cloud Flag Index

Figure 3.21 is a histogram of the resulting index.

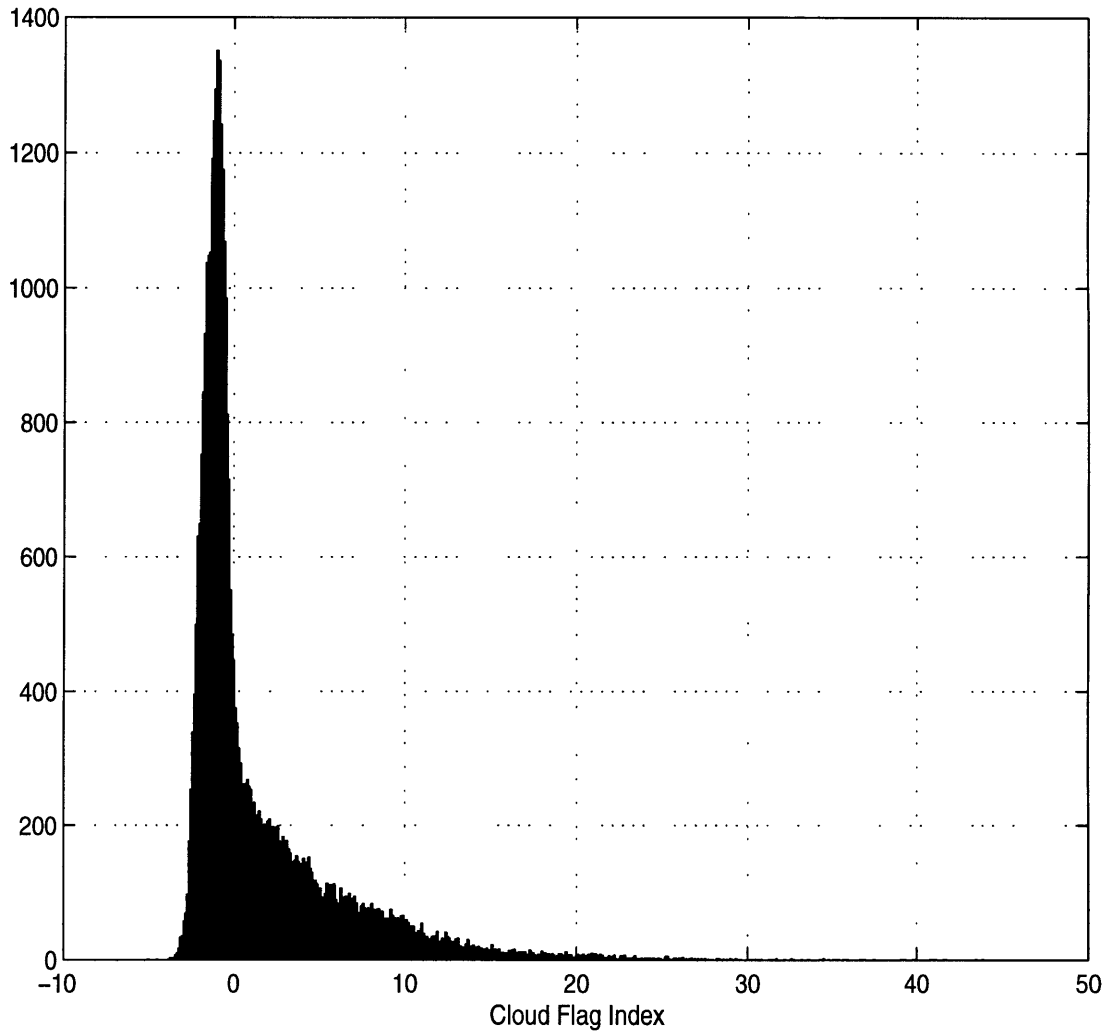


**Figure 3.21:** Histogram of Cloud Flag Index

The histogram of the cloud flag based on the first post-constraint principal component had two large spikes. The histogram of the cloud flag based on the first two post-constraint principal components has only one. As a result, one can conclude that the two spikes in the first histogram resulted from different physical temperatures. The dividing line between regions of cloud cover and regions of clear air is consistent with the expectation that cloud cover is a rare event. The new cloud flag index correctly characterized regions of warm

clear air and those of cool clear air. The region that the first cloud flag incorrectly characterized in Figure 3.17 is correctly characterized by the new cloud flag (Figure 3.22).

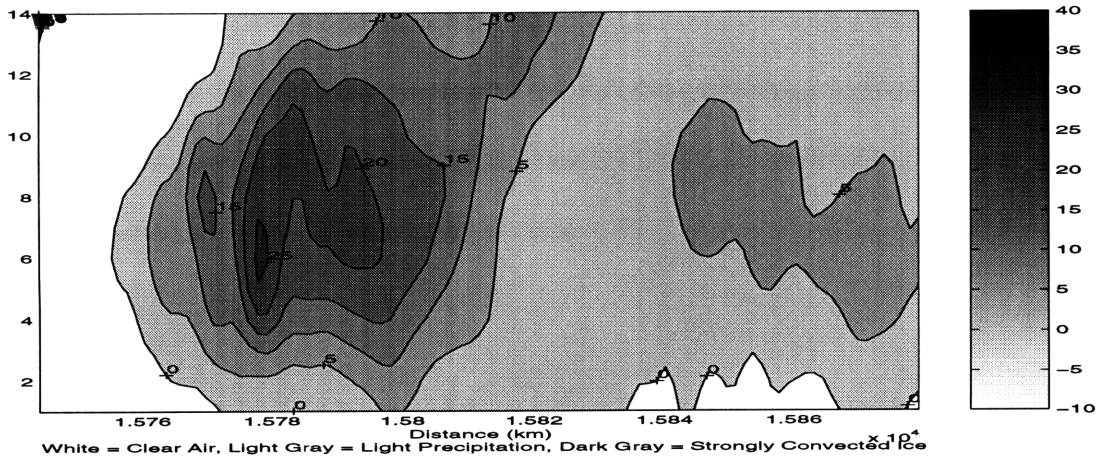


**Figure 3.22:** Plot of Cloud Flag Index in Cloudy Air

# Chapter 4

# Conclusion

## 4.1 The Quality of the Cloud Flag

The results of applying the cloud flag to the data from the flights on October 5, 1993, September 26, 1993, and October 3, 1993, are shown in Appendixes A, B, and C, respectively. For all three flights, values of the cloud flag index were computed using the brightness temperature averages and the eigenvectors that were computed for the flight on October 5, 1993. For the flights on October 5, 1993, and September 26, 1993, the cloud flag based on the first two post-constraint principal components seemed to be a good indicator of cloud cover. It did not respond to surface variations nor did it respond to temperature variations. Regions that are clearly cloud-free and those that have heavy cloud cover were correctly characterized.

However, the cloud flag did not work as well for the data from the flight on October 3, 1993. A discussion of the results for that flight is presented in Appendix C. The line that divided data for cloud-free regions from that for cloudy regions on the scatter plot of the first two post-constraint principal components had to be shifted, and even after the line was shifted, the flag still incorrectly characterized some regions. Differences in the calibrations for each flight might have contributed to the errors in the cloud flag.

## 4.2 Possibilities for Future Research

### **4.2.1** A Nonlinear Cloud Flag Index

The cloud flag developed was a linear combination of the first two post-constraint principal components. The cloud flag might be improved by allowing it to have nonlinear components.

### 4.2.2 Using More Information

The new MTS has a nine-channel scanning 53.65-GHz radiometer in addition to an eight-channel scanning 118.75-GHz radiometer. Like 118.75 GHz, 53.65 GHz is also a resonance frequency of the oxygen molecule $O_2$. The additional information will enable more accurate temperature profile retrievals and much more sensitive detection of clouds. Future MTS's might also include a 380-GHz or a 425-GHz radiometer. 380 GHz and 425 GHz are resonance frequencies of the water molecule $H_2O$ and the oxygen molecule $O_2$, respectively (Staelin 1997).

## 4.3 Constrained Principal Components Analysis

Constrained principal components analysis seems to be a useful technique for isolating degrees of freedom in a data set. In general, data sets often will involve degrees of freedom that are independent based on physical grounds but for unknown reasons produce correlated effects. There is no reason to think that there is any correlation between cloud cover and surface variations. However, after the first attempt to use principal components analysis on the brightness temperature deviations, the first principal component showed the effects of not only clouds but also those of surface variations. On the other hand, undesired effects can be removed from the data. The surface variation eigenvector was determined by doing principal component analysis on only data that came from cloud-free regions of different surfaces. Then, the component of the data spanned by the surface variation eigenvector was removed, and principal components analysis was done on the resulting data. The first principal component of that data, the first post-constraint principal component, was sensitive to clouds but not to surface variations.

# Appendix A

# Analysis of Data From Flight of October 5, 1993

The following are contour plots of the cloud flag index for all of the flight (except for the ascent and the descent) on October 5, 1993.

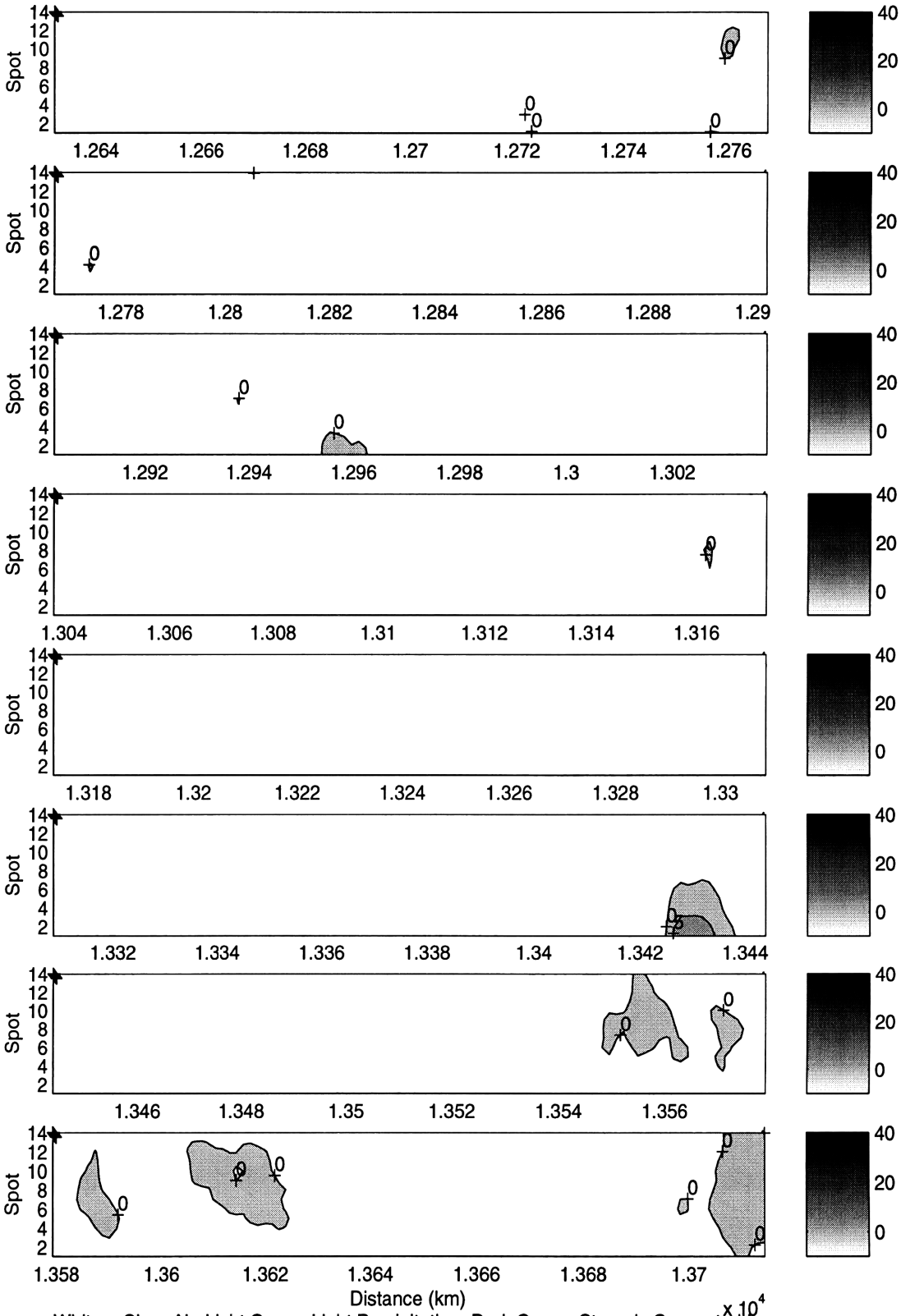


White = Clear Air, Light Gray = Light Precipitation, Dark Gray = Strongly Convected Ice

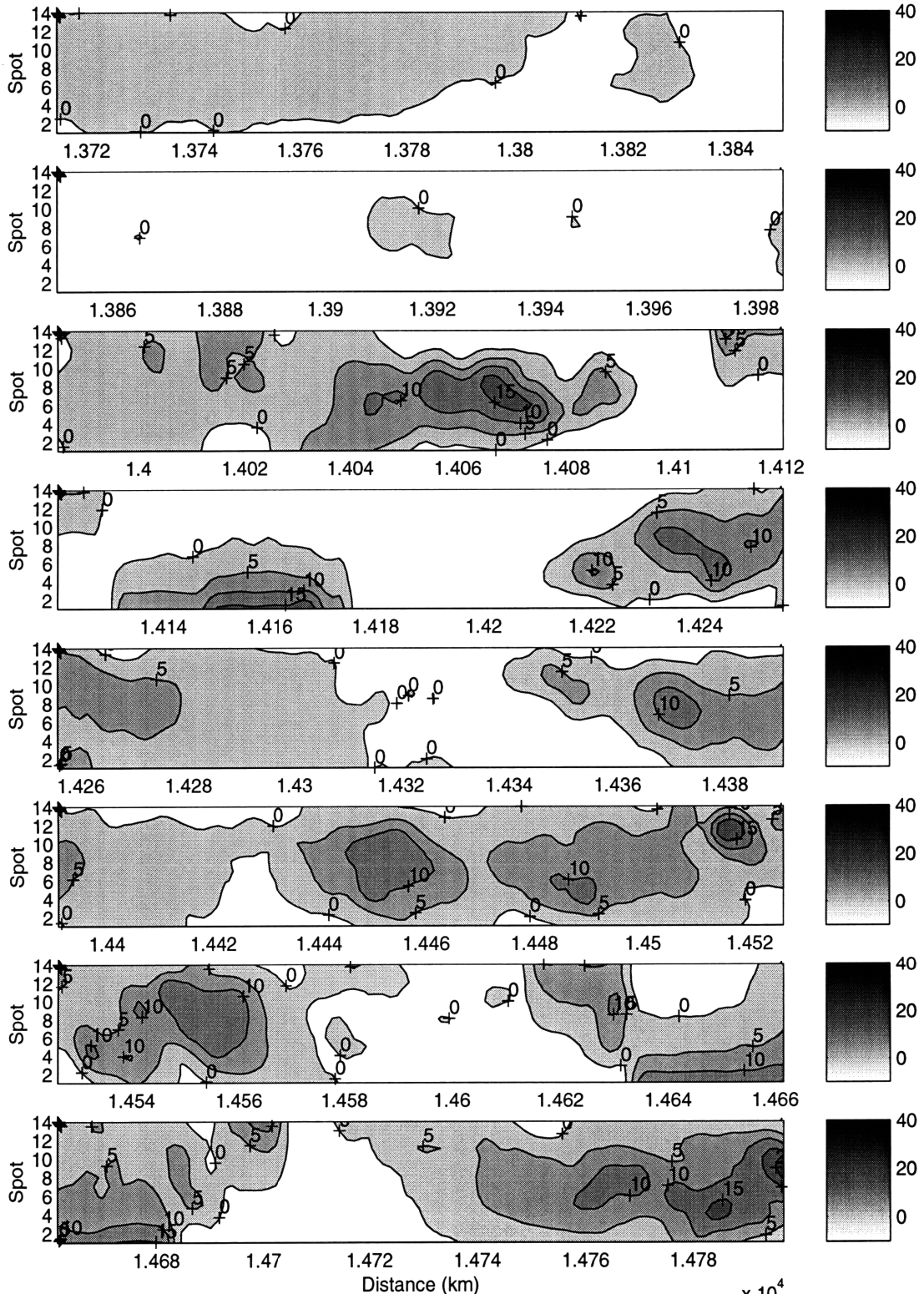
Spot
Distance (km)
x 10^4
White = Clear Air, Light Gray = Light Precipitation, Dark Gray = Strongly Convected Ice

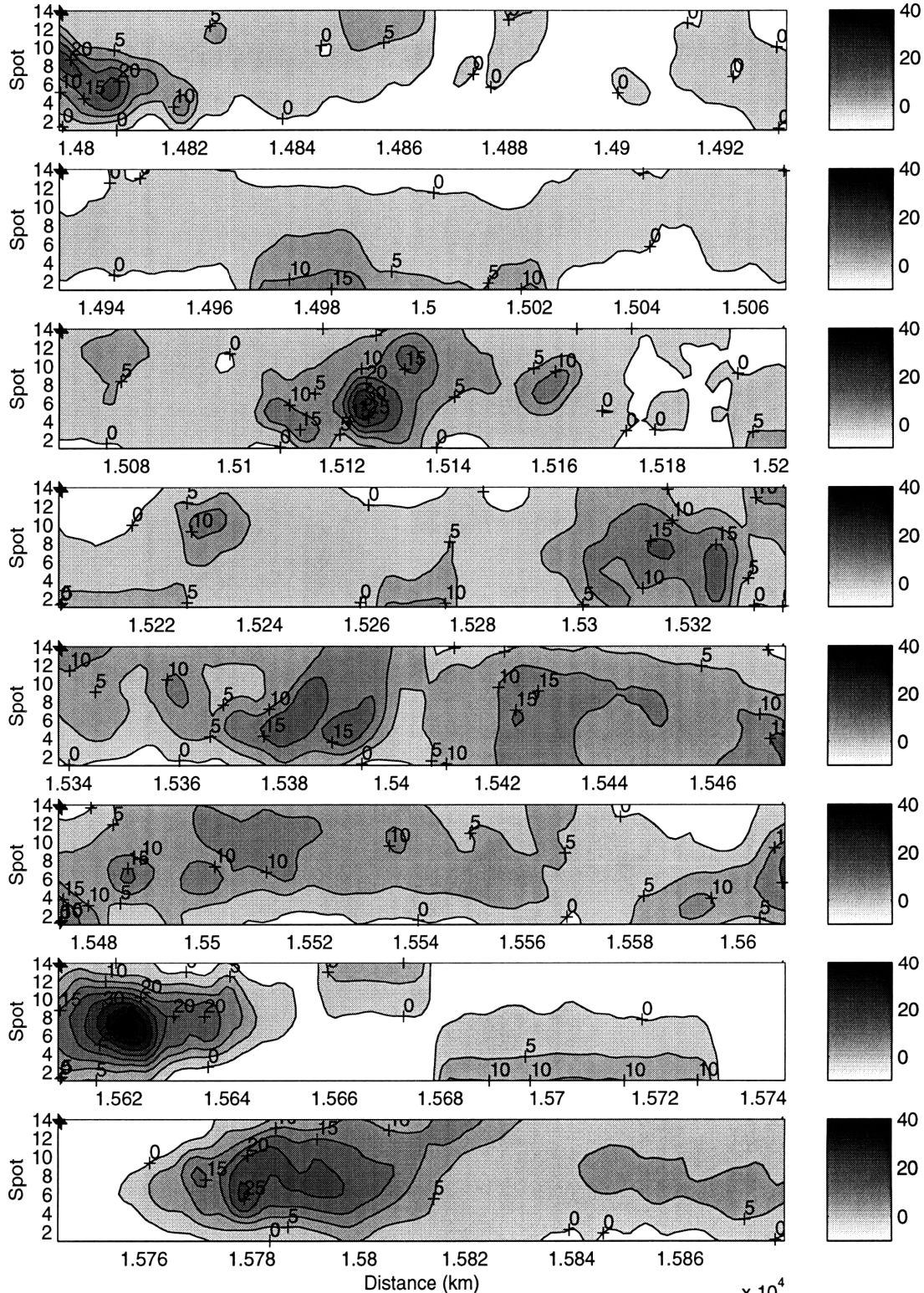


White = Clear Air, Light Gray = Light Precipitation, Dark Gray = Strongly Convected Ice

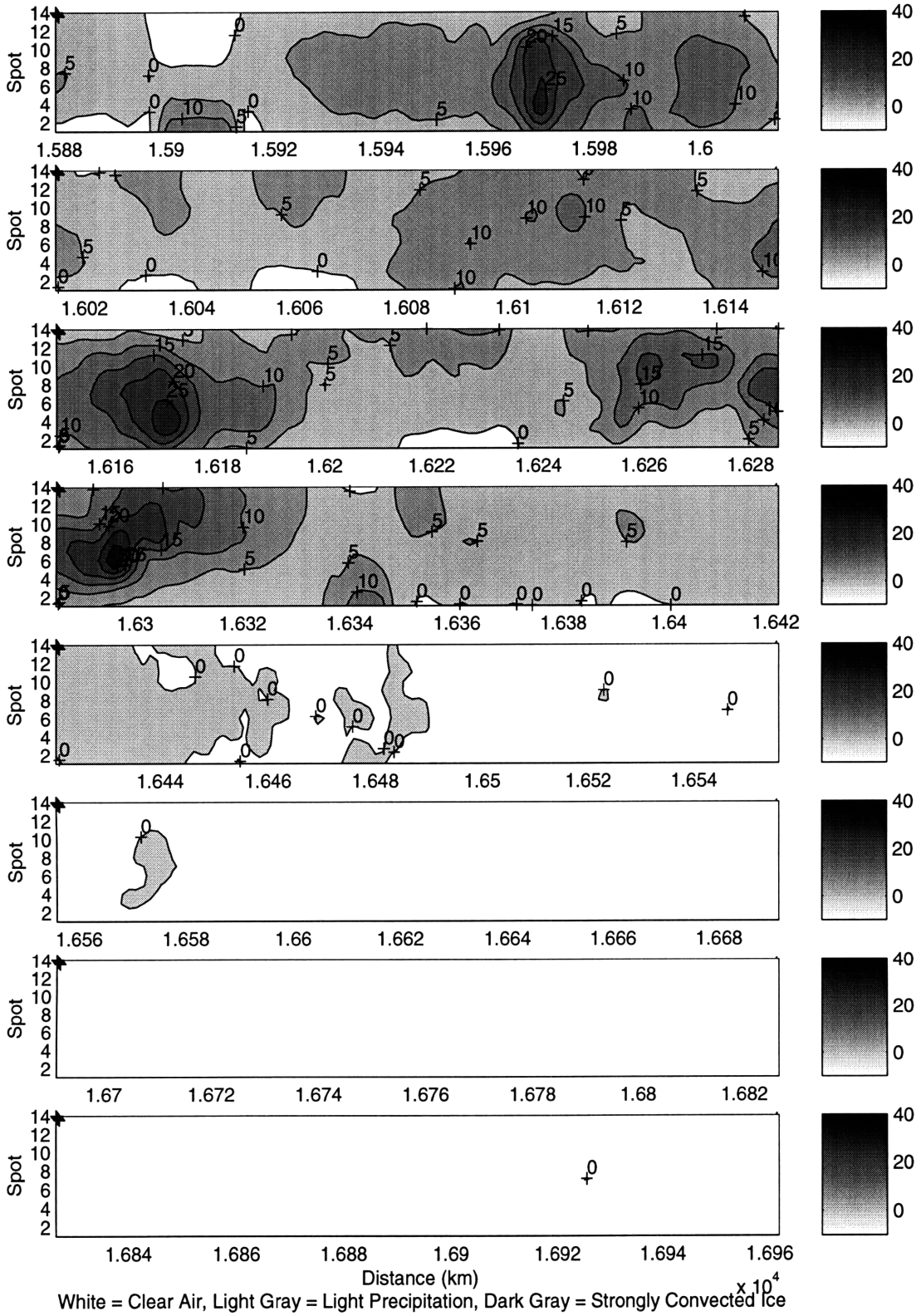
Spot
Distance (km)
x 10^4
White = Clear Air, Light Gray = Light Precipitation, Dark Gray = Strongly Convected Ice

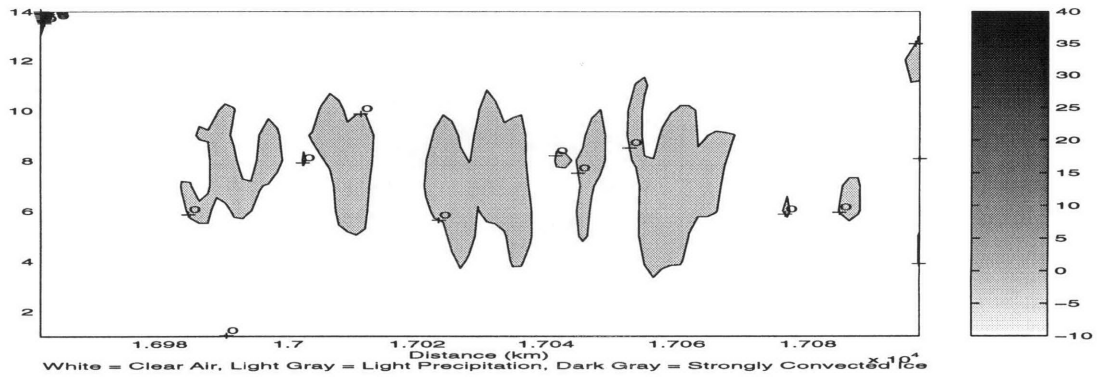
14
12
10
8
6
4
2
1.698
1.7
1.702
1.704
1.706
1.708
Distance (km)
x 10^4
40
35
30
25
20
15
10
5
0
−5
−10
White = Clear Air, Light Gray = Light Precipitation, Dark Gray = Strongly Convected Ice

# Appendix B

# Analysis of Data From Flight of September 26, 1993

The cloud flag that was developed in Chapter 3 was applied to the data collected on this flight. The following are contour plots of the cloud flag index. All of the indicated clouds after 16120 km are due to aircraft roll.

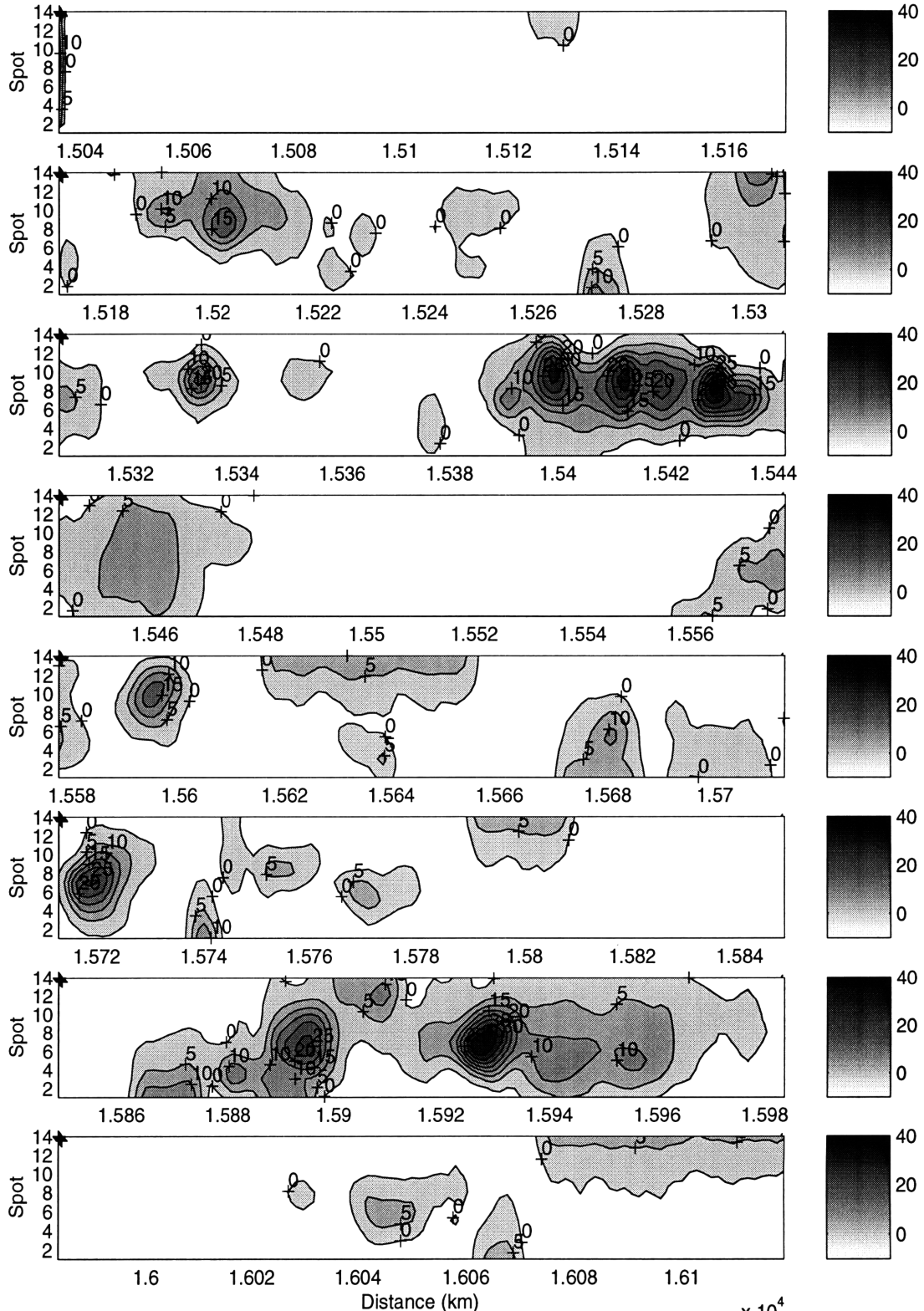
Spot
Distance (km)
x 10^4
White = Clear Air, Light Gray = Light Precipitation, Dark Gray = Strongly Convected Ice

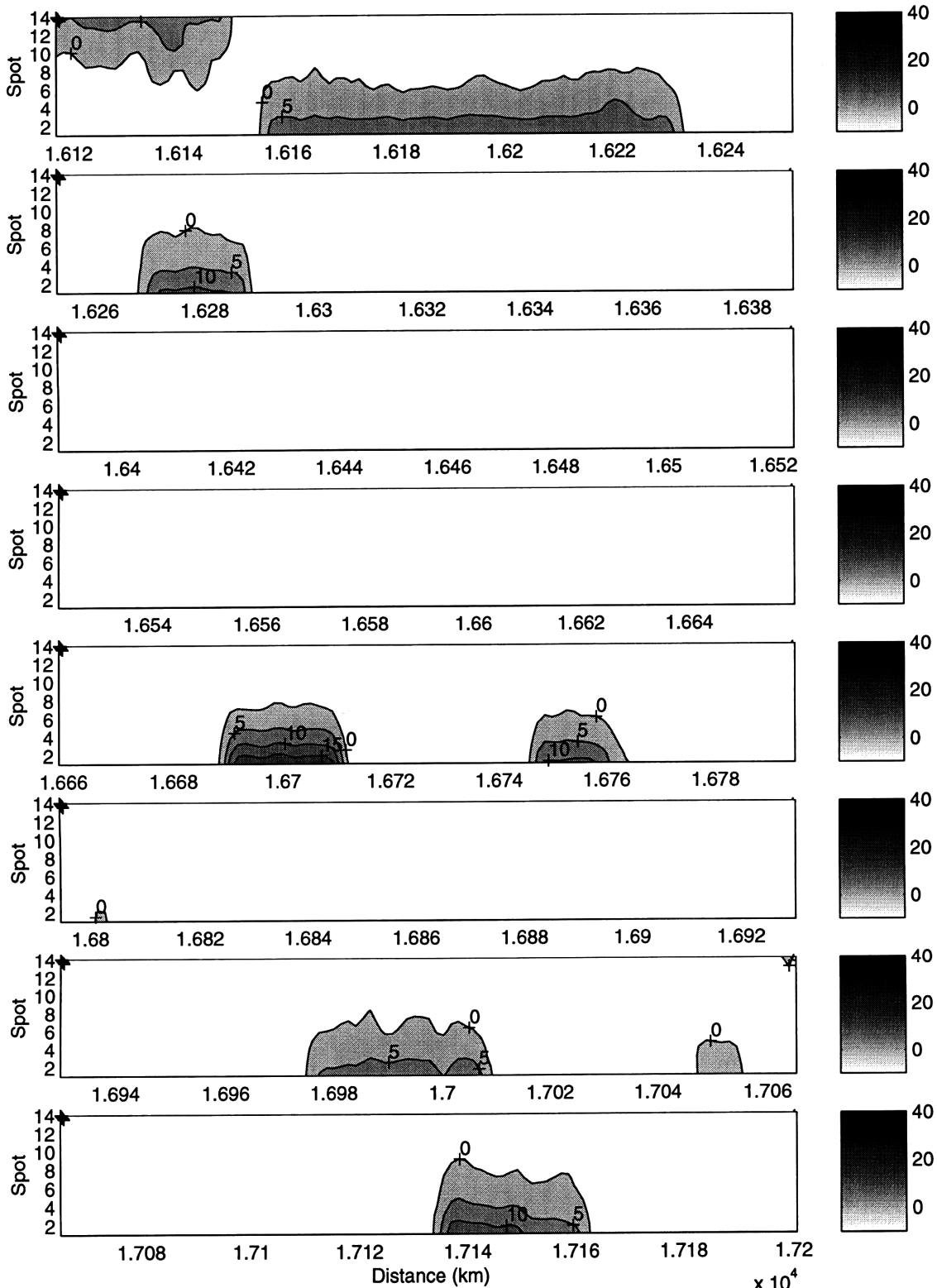
Spot
Distance (km)
x 10^4
White = Clear Air, Light Gray = Light Precipitation, Dark Gray = Strongly Convected Ice

# Appendix C

# Analysis of Data From Flight of October 3, 1993

## C.1 Statistical Analysis of the Data

The cloud flag index developed in Chapter 3 was applied to the data collected for this flight. The index characterized as cloudy some regions that were clearly cloud free. Figure C.1 shows a scatter plot of the first and second post-constraint principal components in clear air. It also shows the original line that separated the data of cloud-free regions from that of cloudy regions.

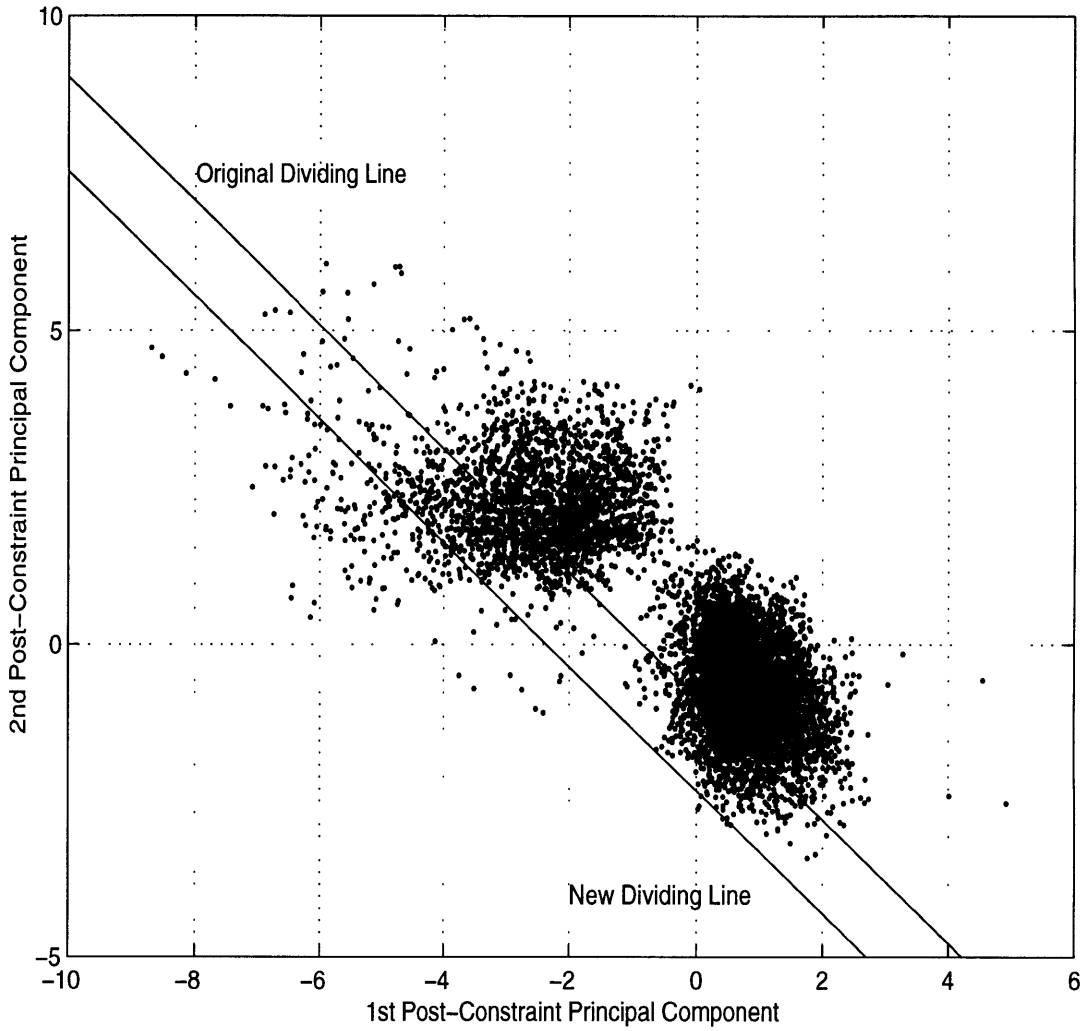


**Figure C.1:** Scatter Plot of First Two Post-Constraint Principal Components in Clear Air

The original dividing line passes through the middle of the two major clusters of points. This might be a result of differences in the calibrations for each flight. The dividing line must be shifted in the direction of increasing the index, which in this case is (-1, -0.9863). The new dividing line results in the following index:

$$\text{Cloud flag index} = y + 0.9863\,x + 2.3350 \qquad \text{(C.1)}$$

where x and y are the first and second post-constraint principal components, respectively. Figure C.2 shows the histogram of this cloud flag index.

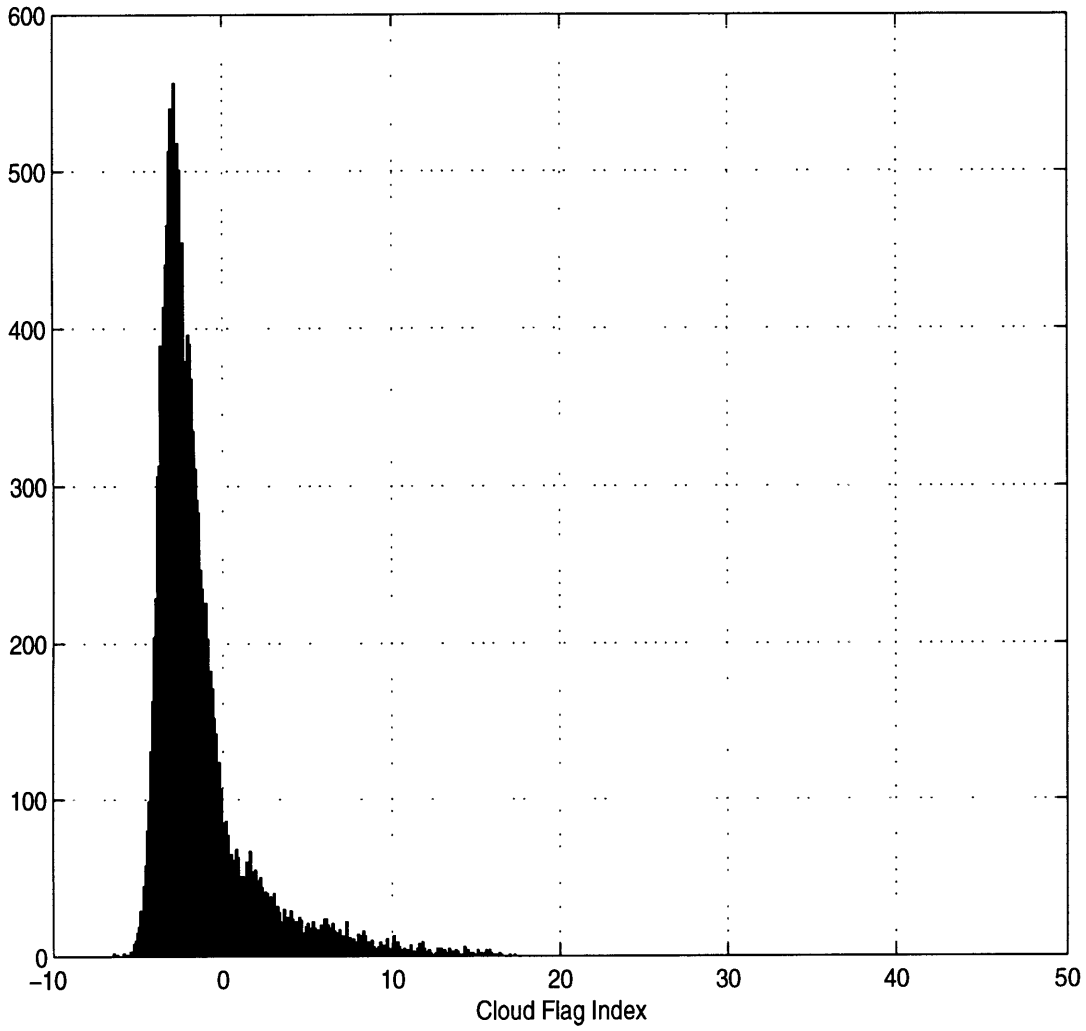


**Figure C.2:** Histogram of Cloud Flag Index

The spike appears to the left of zero and ends at zero. This is consistent with the expectation that cloud cover is rare.

## C.2 Plots of the Cloud Flag

The cloud flag with the new dividing line is better than that with the original dividing line. However, it still characterizes some cloud-free regions as cloudy. Better cloud flags might be developed by changing the slope of the dividing line or introducing non-linear components in the cloud flag index.

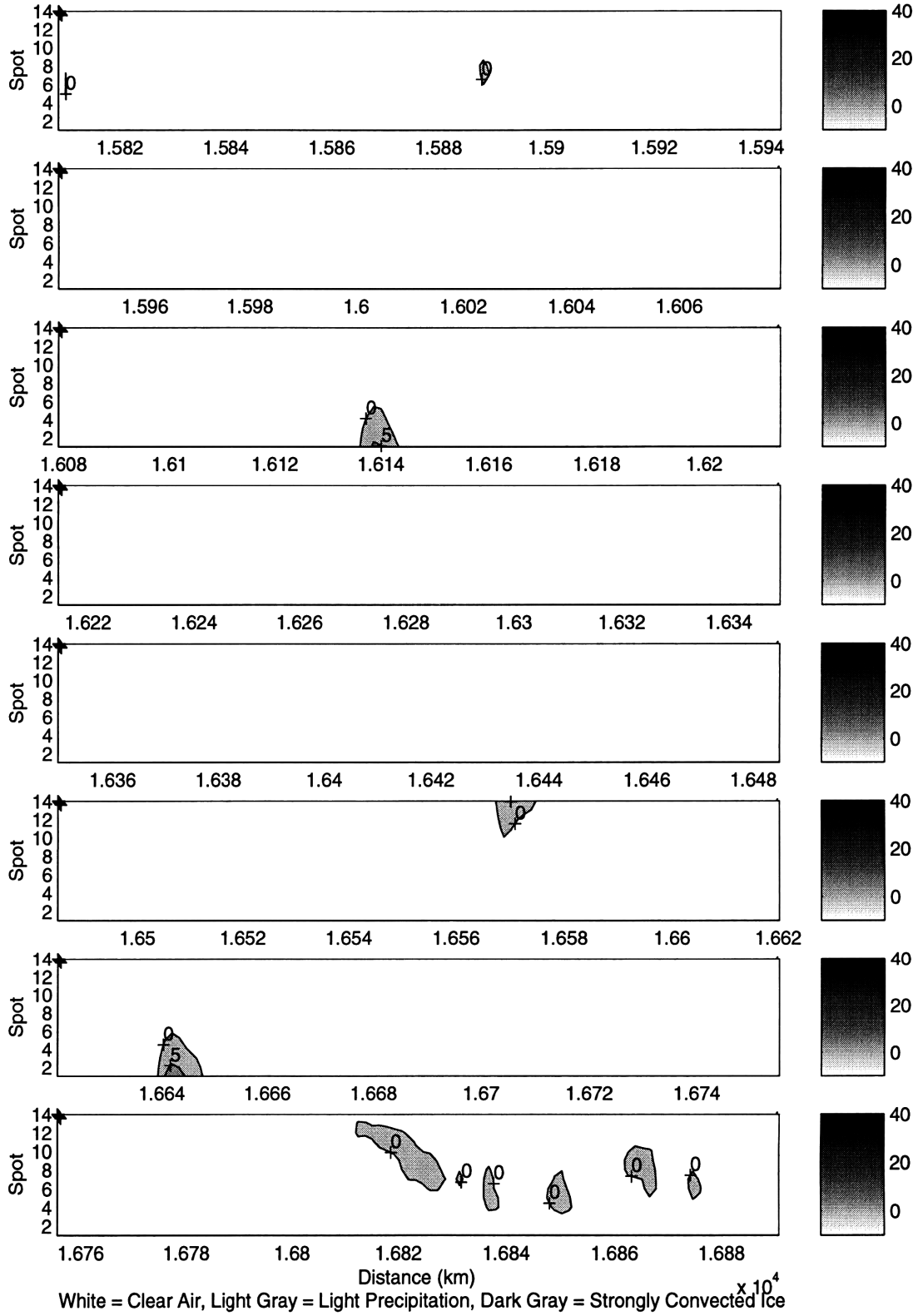


White = Clear Air, Light Gray = Light Precipitation, Dark Gray = Strongly Convected Ice

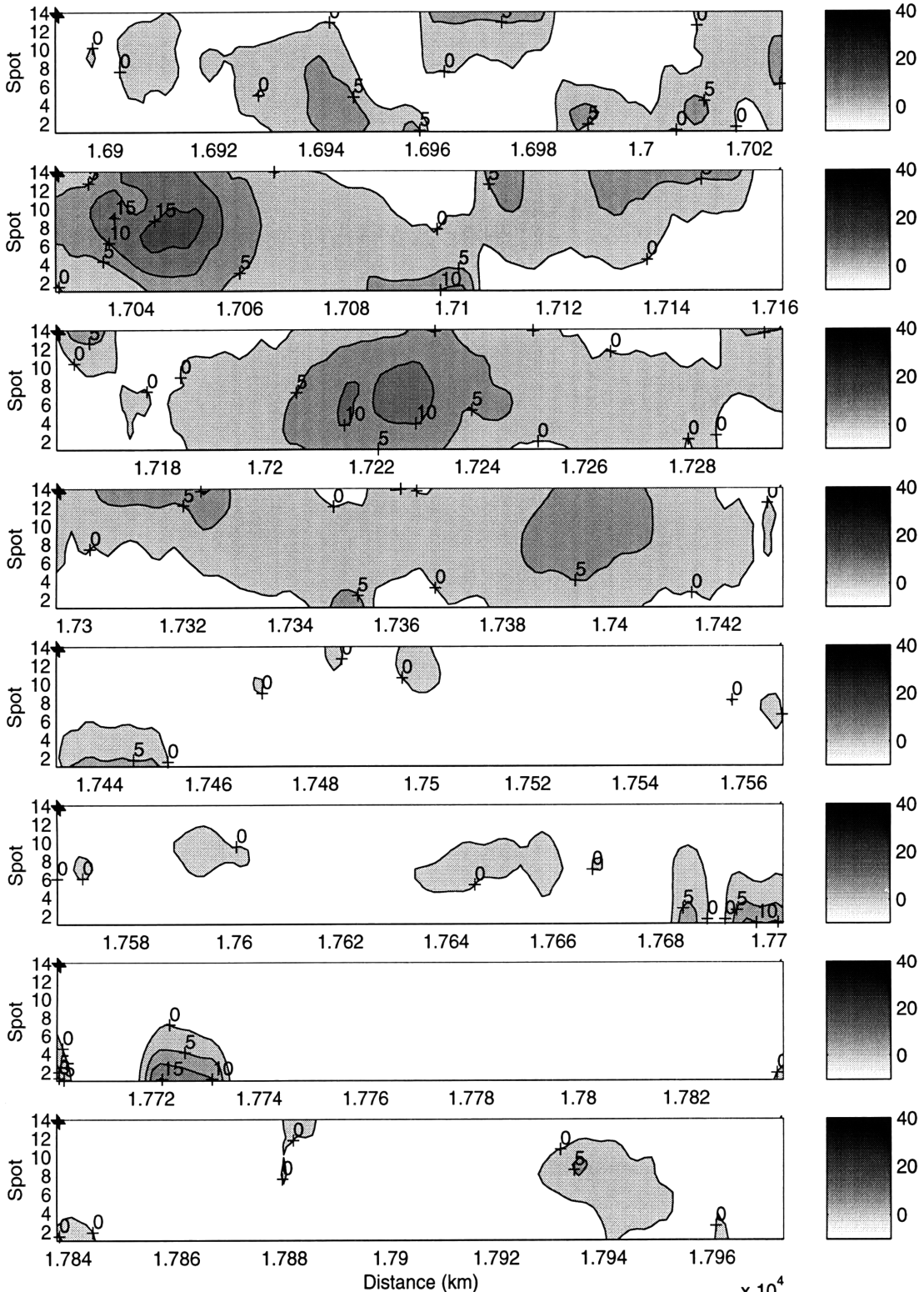
Spot
Distance (km)
x 10^4
White = Clear Air, Light Gray = Light Precipitation, Dark Gray = Strongly Convected Ice

# References


Gasiewski, A. J., J. W. Barrett, P. G. Bonanni, and D. H. Staelin. "Aircraft-based Radiometric Imaging of Tropospheric Temperature and Precipitation Using the 118.75-GHz Oxygen Resonance." *Journal of Applied Meteorology*, Vol. 29, No. 7, pp. 620-632, July 1990.

Helstrom, Carl W. *Probability and Stochastic Processes for Engineers*. Macmillan, 1991.

Nathan, K. S., P. W. Rosenkranz, and D. H. Staelin. "Temperature Profile Retrieval by Two-Dimensional Filtering." *Journal of Climate and Applied Meteorology*, Vol. 24, No. 6, pp. 517-524, June 1985.

Schwartz, M. J., J. W. Barrett, P. W. Fieguth, P. W. Rosenkranz, M. S. Spina, and D. H. Staelin. "Observations of Thermal and Precipitation Structure in a Tropical Cyclone by Means of Passive Microwave Imagery Near 118 GHz." *Journal of Applied Meteorology*, Vol. 35, No. 5, pp. 671-678, May 1996.

Staelin, D. H., A. L. Cassel, K. F. Kunzi, R. L. Pettyjohn, R. K. L. Poon, and P. W. Rosenkranz. "Microwave Atmospheric Temperature Sounding: Effects of Clouds on the Nimbus 5 Satellite Data." *Journal of Atmospheric Sciences*, Vol. 32, No. 10, pp. 1970-1976, October 1975.

Staelin, David H. "The Detection and Measurement of Radio Astronomical Systems." Lecture notes for subject 6.661. MIT Department of Electrical Engineering and Computer Science, Fall 1974.

Staelin, David H. Personal communication, 1997-1998.

Tsang, Leung, Jin Au Kong, and Robert T. Shin. *Theory of Microwave Remote Sensing*. John Wiley and Sons, 1985.